HERON is jointly edited by:
STEVIN-LABORATORY of the
faculty of Civil Engineering,
Delft University of Technology,
Delft, The Netherlands
and
TNO-INSTITUTE
FOR BUILDING MATERIALS
AND STRUCTURES.
Rijswijk (ZH), The Netherlands
HERON contains contributions
based mainly on research work
performed in these laboratories
on strength of materials, structures
and materials science.

ISSN 0046-7316

EDITORIAL BOARD:
J. Witteveen, *editor in chief*
G. J. van Alphen
R. de Borst
J. G. M. van Mier
A. C. W. M. Vrouwenvelder
J. Wardenier

Secretary:
G. J. van Alphen
Stevinweg 1
P.O. Box 5048
2600 GA Delft, The Netherlands
Tel. 0031-15-785919
Telex 38070 BITHD

HERON vol. 33
1988
no. 4

Contents

THEORETICAL AND EXPERIMENTAL ANALYSIS OF THE BEHAVIOUR OF CRACKED CONCRETE UNDER MONOTONIC AND CYCLIC SHEAR LOADING

A. F. Pruijssers
Dirk Verstoep bv
formerly Delft University of Technology, Stevin-laboratory

This publication has been issued in close co-operation with the Centre for Civil Engineering Research, Codes and Specifications

Summary

The safety against failure of large and slender structures, such as offshore platforms, is analyzed by means of advanced finite element programs. An offshore platform is designed to withstand severe loading conditions, characterized by wave, wind and ice attacks. The basement of the structure is so configured as to transfer the applied loads by means of in-plane shear and normal stresses. The shear walls in the basement might be cracked due to unequal settlements and deformations, thus responding in a highly non-linear way to the applied loads. To make an accurate estimate of the structure's actual safety against failure, this non-linear behaviour must be thoroughly analyzed and implemented in the finite element program. The basement is subjected to static loads on which cyclic loads are superimposed. In the case of the cyclic loads, a distinction is usually made between "low-intensity high-cycle" loading, reflecting millions of small wave attacks and "high-intensity low-cycle" loading, reflecting a superstorm.

Experimental and theoretical studies performed by several researchers have revealed that the transfer of in-plane stresses across cracks in reinforced concrete is based on the axial and lateral stiffness of the reinforcing bars and the interlocking of the aggregate particles protruding from the crack faces.

From literature research it has become clear that there was a lack of experimental knowledge on the response of cracked reinforced concrete to a large number of shear load reversals with a low shear stress relative to the static shear strength. Therefore, an experimental study was carried out with plain concrete and reinforced concrete push-off specimens. After pre-cracking, the specimens were subjected to a repeated shear stress ranging from 46 to 90% of the static shear strength. The number of cycles varied between 118 and 931.731 cycles. The relationship between stress level and crack displacements is expressed in empirical relations.

These expressions can be used to provide a quasi-static description of the load history of millions of small wave attacks. In consequence, the crack response under monotonic loading must be fully understood. Whereas the interlocking of the particles, the aggregate interlock, was satisfactorily described by the two-phase model of Walraven. The lateral stiffness of the bars had not yet been properly described.

Therefore, a physical description of the so-called dowel action based upon the cooperation of the steel bar and the supporting concrete was given.

It is shown that the combined mechanism of aggregate interlock and dowel action transfers the monotonically applied shear stress across cracks in reinforced concrete. Furthermore, the crack opening path was found to be initially influenced by the bars. After plastic hinges in the bar have fully been developed, the aggregate interlock mechanism determines the crack opening direction.

In the case of cyclic shear loading, Walraven's two-phase model was extended and simplified to obtain the reduced contact model. This quasi-statical model is used to simulate several "high-intensity low-cycle" experiments.

The cyclic dowel action mechanism is described by means of a rather simple model, which is to a large extent based upon empirical relations.

Again, the combined model of aggregate interlock and dowel action provided a good prediction of the crack response in reinforced concrete for the case of "high-intensity low-cycle" experiments.
Furthermore, a few cycles of "high-cycle" tests are satisfactorily predicted. An important conclusion was that the contributions to the shear transfer of both mechanisms remain nearly constant during cycling.
On the basis of this observation it was possible to predict the crack opening path for the case of "low-intensity high-cycle" loading.

Theoretical and experimental analysis of the behaviour of cracked concrete under monotonic and cyclic shear loading

1 Introduction

The tremendous increase in material science as well as the development of new materials enables the construction of slender structures which are still capable of withstanding the applied loads.
The safety against failure of such complex structures is analyzed by idealizing the structure as an assemblage of basic elements. Advanced finite element programs are used to simulate the interactions of these elements.
Due to the applied loads and deformations, structural elements are subjected to tensile stresses which exceed the tensile strength, thus causing cracking of the concrete. Furthermore, cracking of the concrete might be caused by colliding objects.
The considerable stiffness of cracked reinforced concrete is then utilized in withstanding the applied loads and deformations during the economic lifetime of the damaged structure. Moreover, it can be favourable to design a structure in such a way that cracked structural elements provide a large ductility with respect to unequal settlements. As a consequence of the development of cracks, the response of the elements to severe loading conditions becomes highly non-linear with large irreversible deformations.
This non-linear material behaviour must be thoroughly understood and modelled. It was for this reason that the "Concrete Mechanics" project was initiated by the Netherlands Centre for Civil Engineering, Research, Recommendations and Codes (CUR). This project comprises experimental research, material modelling and their implementation in numerical programs.
The "Concrete Mechanics" project is a cooperative project involving a division of the Netherlands Ministry of Transport and Public Works (Rijkswaterstaat), the Institute for Applied Scientific Research on Building Materials and Building Structures (IBBC-TNO) and the Technical Universities of Delft and Eindhoven.
The first phase of the project focussed upon the investigation of the behaviour of cracked reinforced concrete under static shear loads, the bond behaviour of reinforcing bars, the creep of concrete in a marine environment and multiaxially loaded concrete. Furthermore, two non-linear finite element programs (MICRO, DIANA) were developed. The current study forms part of the second phase of the "Concrete Mechanics" project and deals with the response of cracked reinforced concrete to cyclic in-plane shear loads.
A large number of tests [17, 20, 24, 49] were conducted with a rather large initial crack width and a relatively high shear load.
These so-called "high-intensity low-cycle" tests especially reflected the pattern of

earthquake motions. For instance offshore structures are subjected to millions of load cycles due to wind, wave and ice attacks. These load cycles have a relatively low amplitude with respect to the static shear strength of the (cracked) shear panels, which form the basement.
These "low-intensity high-cycle" loads might cause gradually increasing irreversible deformations, thus influencing the strength and stiffness of the structure in the case of subsequent higher loads.
Since there is still a lack of information with respect to this type of tests an experimental study was conducted with "low-intensity high-cycle" loading.
The aim of the research is to determine the relationship between the stresses and displacements in the crack plane.
This relationship largely depends upon the roughness of the crack faces and the dowel action. The roughness is caused by the contact between the matrix material and the aggregate particles protruding from the crack faces. This mechanism is referred to as aggregate interlock.
Both the aggregate interlock and dowel action mechanisms are strongly influenced by the interaction of the normal and lateral forces acting on the crack plane. Hence the relationship between the stresses and displacements must reflect this interaction between tension-softening and shear-softening. However, this interaction is generally not taken into account in numerical programs.
Therefore, a sound description of the physical transfer mechanisms is presented and a simplified model is derived for implementation in numerical programs.

2 Survey of the literature

2.1 *Introduction*

The major transfer mechanisms in cracked reinforced concrete are aggregate interlock, dowel action of the reinforcing bars and the axial steel stress in the bars, see Fig. 2.1.
These mechanisms will be discussed separately. In the case of cracked reinforced concrete, the interaction of the mechanisms is discussed.
The survey is limited to experimental results reported in the literature.
Existing empirical and physical models are discussed in Chapter 4.

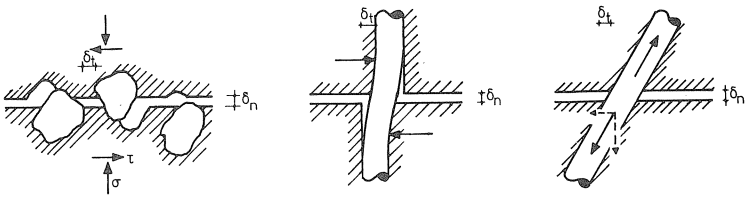

Fig. 2.1. Major transfer mechanisms in cracked reinforced concrete.

2.2 *The aggregate interlock mechanism*

The role of aggregate interlock in shear transfer in cracked concrete was first reviewed by Taylor [39] and Moe [29].
It was, however, Fenwick [10] who carried out the first detailed theoretical and experimental study into this mechanism and described it as aggregate interlock.
This study as well as the subsequent surveys by various investigators [5, 7, 15, 26, 30, 31, 38, 47, 50] revealed that the static shear strength of plain concrete is proportional to the square root of the concrete compressive strength.
Furthermore, the type of aggregate influences both the shear strength and the crack opening path (for a constant normal restraint stiffness).
The maximum particle diameter, ranging from 8 to 32 mm, hardly influences the static shear strength, but does affect the crack opening direction.
A study into the aggregate interlock mechanism as regards cyclic shear loading was first carried out by Colley and Humphrey [4]. The specimen tested consisted of two concrete slabs based upon a subsoil. The joint resistance to shear load was investigated for variations in joint width, load level, aggregate type and the quality of the subsoil.
This type of test, however, dit not represent the situation of cyclic in-plane shear loading.
Experimental work with in-plane shear loads focussed on the "low-cycle high-intensity" behaviour, exploring the response of cracked nuclear containment vessels subjected to earthquake motions.
Such tests were conducted by White and Holley [55].
A total of sixteen specimens were pre-cracked and loaded to transmit shear by the crack roughness. The shearing area was 180645 mm^2. The test variables were the size and gradation of the aggregate, the normal restraint stiffness provided by external bars, the shear stress level, the number of cycles and the initial crack width.
The test results were used to make a first assessment of the crack response to cyclic loading.
On the basis of these results, Laible et al. [20] performed further tests with a push-off specimen as shown in Fig. 2.2. For this pre-cracked specimen, the shearing area was 194000 mm^2.

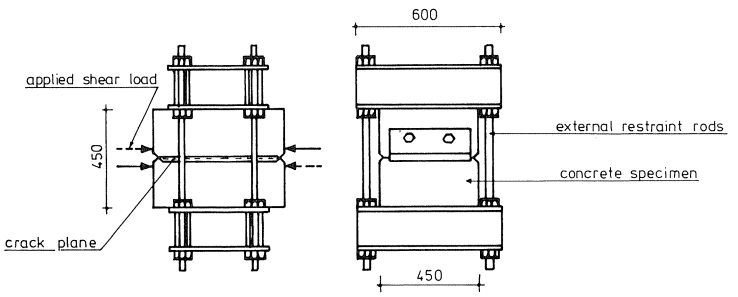

Fig. 2.2. Test arrangement used by Laible et al. [20].

The concrete cylinder strength was 20.7 MPa for the major series, the maximum particle size was equal to 38 mm.
In addition to the variables used in White's test series [55] the specimen geometry and the strength and the age of the concrete were varied in the tests.
For an adjusted initial crack width of 0.25, 0.51 or 0.76 mm, a fully reversed load of 1.24 MPa was applied to the specimen. Fig. 2.3a, b, c presents a test result which is representative of the generally observed behaviour.

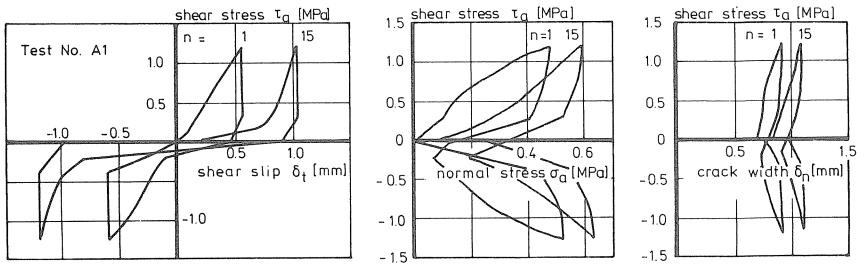

a. Shear stress - shear slip relationship.

b. Shear stress - normal stress relationship.

c. Shear stress - crack width relationship.

Fig. 2.3. Experimental results of Laible et al. [20].

The number of cycles was 25. For the cycles no. 1 and no. 15 the load was applied stepwise, during the other cycles the full load was applied in one step.
The first loading cycle showed a nearly linear relationship between the crack displacements and the shear stress, whereas this relation became highly non-linear for the later cycles. During unloading, the recovery of the shear displacement was approximately 20% of the maximum slip, which was probably due to local irreversible deformation of the contact areas.
Due to the crushing of the matrix material in the previous cycles, the initial stiffness is very low and a "contactless" slip may occur before any contact between the opposing crack faces is possible, see Fig. 2.3a.
Paulay and Loeber [31] carried out both static and repeated shear loading tests on precracked concrete push-off specimens, see Fig. 2.4a.
For the repeated loading experiments, some experimental results are shown in Fig. 2.4b.
The concrete cylinder strength was 37 MPa, the maximum particle size 19 mm. A surprising result was the low shear stiffness during unloading compared with the stiffness during loading. This result deviated from the low recovery in shear displacement during unloading found in the experiments by Laible [20].
Contrary to the constant crack width used in Paulay's tests, the crack width increased with increasing shear displacement in Laible's test. The unloading of the specimen in Paulay's investigation was probably influenced by the high normal stress required to maintain the constant crack width.

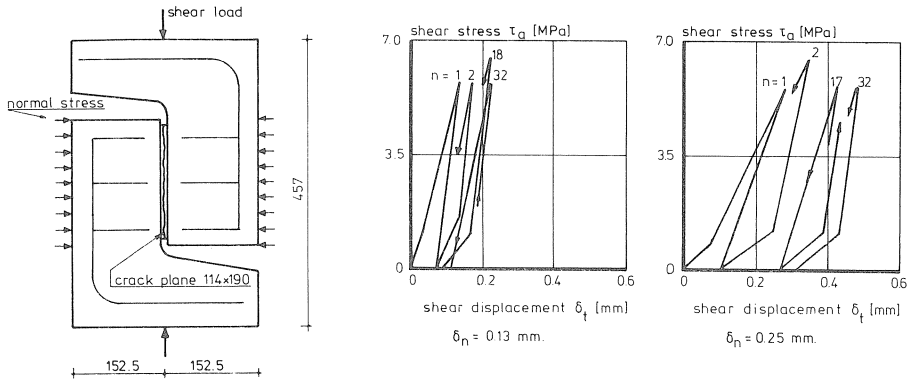

Fig. 2.4. Test specimen and experimental results of Paulay and Loeber [31].

Vintzeleou [46] performed both static and cyclic shear loading experiments with the test arrangement shown in Fig. 2.5a. The cyclic tests were carried out with a fully reversed shear displacement, representing earthquake motions.

Due to the large displacements applied, only a few cycles were used. Fig. 2.5b presents a typical test result for a concrete cylinder strength of 30 MPa and a constant normal stress of 2.00 MPa. The maximum particle diameter was 30 mm.

It was found that for a high normal stress ($\sigma_n \geqq 2.0$ MPa) no degradation of the response occurred.

Chung [3] carried out impact tests on push-off specimens with a shearing area of 18750 mm^2, which consisted of a joint between precast concrete and concrete cast in situ. One test series was performed with specimens which were preloaded with a low intensity shear load during two million cycles. For a load intensity of 55% of the static shear strength, no response degradation was found.

An intensity of 66% caused a decrease in shear strength of 14–20%. It was found that the impact shear strength for a loading rate of 12,000 MPa/s was approximately 80% higher than the static shear strength.

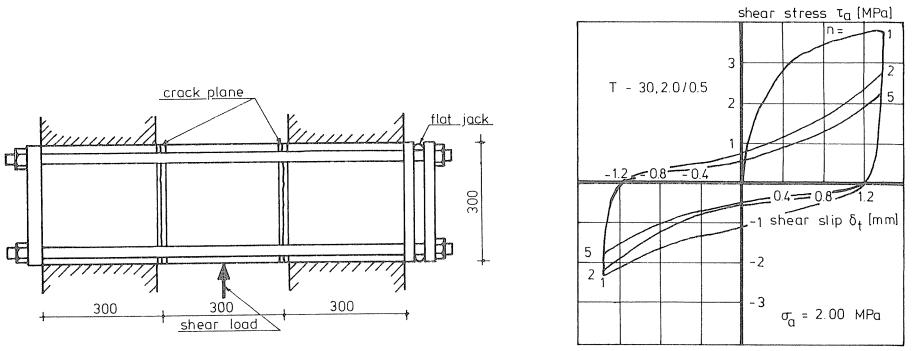

Fig. 2.5. Test arrangement and cyclic test results of Vintzeleou [46].

2.3 *The dowel action mechanism*

A reinforcing bar embedded in concrete counteracts lateral displacements due to crack motions. This lateral stiffness is caused by the reaction stresses of the surrounding concrete and is called dowel stiffness.

Several failure modes can occur in dowel action, including splitting failure of the concrete cover. This type of failure generally occurs in the case of bottom bars in a beam with a small concrete cover. In this case the tensile stresses in the concrete cannot achieve equilibrium with the dowel force. This failure model will not be discussed here.

In the case where adequate confinement is provided to prevent splitting of the concrete cover, the dowel action mechanism fails due to concrete crushing around the bar. Here, the concrete reaction force is relatively high with respect to the stress condition in the surrounding concrete.

As for the aggregate interlock mechanism, the first experimental investigation concerning dowel action focussed on joints in concrete pavements based upon a subgrade [37, 40]. Dowel tests with push-off specimens loaded in static shear were carried out by Paulay et al. [32]. For bars perpendicularly crossing the smooth shearing area, the test arrangement and the test results are presented in Fig. 2.6a and b.

These tests and the experiments reported in [1, 8, 9, 26, 28, 35, 45, 46] revealed that for static loads the dowel action mechanism is characterized by a linear relationship between the dowel stress and the lateral bar displacement. This relationship remains valid for dowel stresses up to 40% of the ultimate dowel stress.

After that the relation between dowel displacement and dowel force becomes nonlinear until the dowel strength is reached. In this case the concrete strength and the steel yield strength strongly influence the ultimate dowel force.

The failure mechanism is characterized by the formation of plastic hinges in the reinforcing bar and local crushing of the concrete under the bar.

Furthermore, the dowel stiffness is affected by the initial crack width and the initial axial steel stress, although these parameters might interfere.

In addition to static tests, numerous cyclic dowel action experiments have been performed.

Test series carried out by Eleiott, Stanton [36] and Jimenez [16] at Cornell University explored the response of a dowel to cyclic shear loads. Some typical results are shown in Fig. 2.7a, b, c.

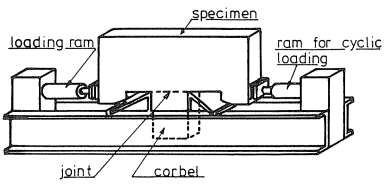

a. Test arrangement

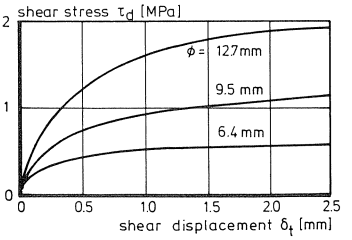

b. Shear stress - shear displacement relationship.

Fig. 2.6. Test arrangement and experimental results of Paulay et al. [32].

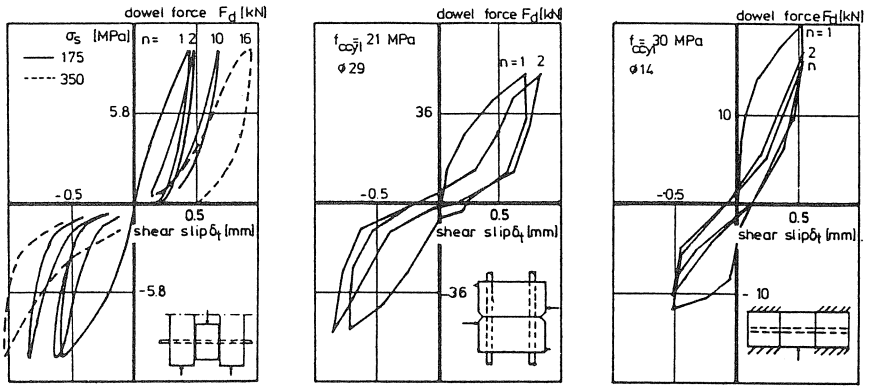

Fig. 2.7. Experimental results of cyclic dowel actions tests [9, 17, 49]

Eleiott investigated the influence of an axial steel stress upon the dowel stiffness. Fig. 2.7a presents a tests result for a bar diameter of 12.6 mm and a concrete strength of 21 MPa with an increased crack width, thus reducing the dowel stiffness with respect to the stiffness of an unstressed bar.

In cycle no. 16, the steel stress was increased to 350 MPa, which again strongly influenced the dowel stiffness. The tests of Stanton and Jimenez with large concrete blocks interconnected by several bars showed a similar response in both loading directions in the case of a fully reversed load.

With the test arrangement used for the aggregate interlock test, Vintzeleou and Tassios [48, 49] performed dowel action tests.

The specimens were subjected to cyclically imposed shear displacements. They found that the dowel force at maximum shear displacement decreased during cycling. This decrease was influenced by the ratio between the displacement in the positive direction and the displacement in the negative direction.

All tests found in the literature were of the "high-intensity low-cycle" type. The test results showed that as for the aggregate interlock mechanism, the dowel response to cyclic loading becomes highly non-linear for subsequent cycles as compared to the response in the first cycle.

2.4 *Axial steel stress*

Reinforcing bars generally cross cracks at different angles. The component of the steel stress parallel to the crack plane provides a contribution to the transfer of shear stress across the crack.

This contribution can easily be determined when the axial steel stress and the angle of inclination are known. The magnitude of the axial steel stress depends upon the bond characteristics.

For bars at angles to the crack plane or bars subjected to both axial and lateral displacements the bond characteristics will be less than is found in pull-out experiments. Due to

the lateral displacement, the bond between the bar and the concrete is broken, which means that the bond capacity will decrease with a decreasing angle of inclination. This was confirmed by Klein [18] who performed displacement-controlled tests with bars at various angles to the crack plane, see Fig. 2.8a.

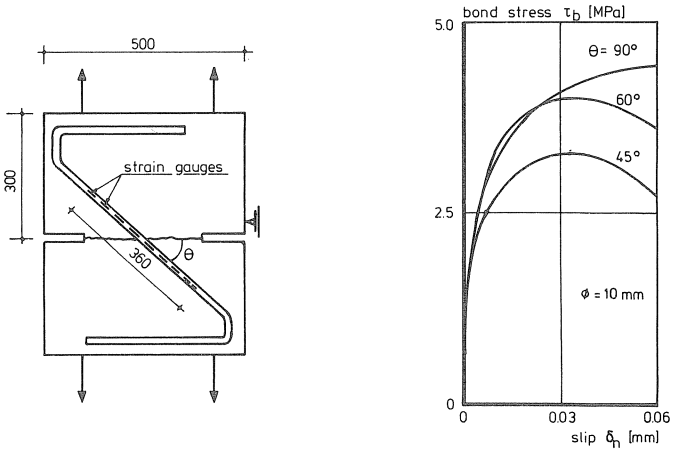

a. Test specimen. b. Bond stress versus slip.

Fig. 2.8. Test arrangement and experimental results of Klein et al. [18].

The variation of steel strains was recorded by strain gauges stuck to the bar. Some typical results are presented in Fig. 2.8b, showing that no systematic variation in bond behaviour for several angles of inclination was obtained in these tests.

2.5 *Shear transfer in cracked reinforced concrete*

For design purposes, a simple shear-friction model was introduced by Mast [21] and Birkeland [2]. According to this model the static shear strength of cracked reinforced concrete was provided by the friction in the shear plane. The applicability of this model was confirmed experimentally by Hofbeck et al. [14]. It was found that the angle of friction was 39° ($\tan(\psi) = 0.8$). Also a cohesion was added, representing the dowel action:

$$\tau_u = 2.8 + 0.8(\varrho f_{sy} + \sigma_n) \tag{2.1}$$

In further tests, Mattock [22] found that the small aggregate particles must have a large influence upon the crack opening direction.
Walraven [50, 54] conducted static tests on cracked reinforced push-off specimens, see Fig. 2.9a.
The measured crack opening paths appeared to be insensitive to variations in the bar diameter, and the reinforcement ratio see Fig. 2.9b. However, the number of bars strongly influenced the shear strength, see Fig. 2.9c.

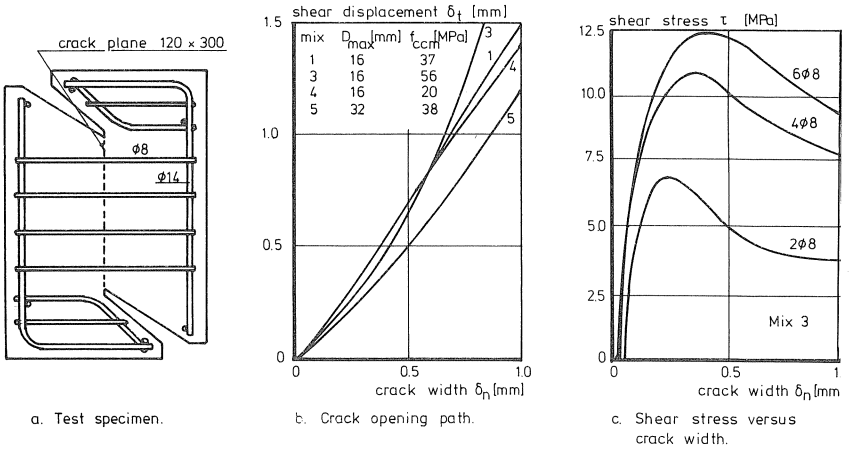

a. Test specimen. b. Crack opening path. c. Shear stress versus crack width.

Fig. 2.9. Test specimen and experimental results of Walraven [54].

Similar tests performed by Millard [27] confirmed Walraven's results. The constant crack opening direction found by Millard deviated from the average crack opening path obtained by Walraven.

Jimenez [17] performed cyclic push-off tests on cracked reinforced concrete. The crack response depended on the initial crack width and the applied shear stress level. It must be noted that an increase in crack width is accompanied by an increasing axial steel stress.

Mattock [24] carried out cyclic tests on a specimen with a reinforcement ratio ranging from 0.60% to 1.32%.

During unloading the response was characterized by a retention of almost all the shear displacement under maximum shear stress until the shear stress was reduced to approximately 50% of its maximum value.

A decrease in crack width at zero shear stress was observed. This decrease amounted 0.08–0.13 mm as against an initial crack width of 0.25 mm. This crack width remained constant until shortly before failure. From the tests it was found that for the cyclic test on lightweight concrete, the shear slip was larger and the crack width was smaller than those measured in the monotonic test at the same shear stress. For the normal gravel concrete, the displacement in the cyclic tests was approximately equal to the slip in the static test. However, at a shear stress level of 80% of the static shear strength, the slip rapidly increased. The same held true for the crack width.

2.6 *Concluding remarks*

The experiments reported in the literature revealed that the crack response to cyclic loads is influenced by the concrete strength, the yield strength of the reinforcing steel, the initial crack width and the shear stress level. The available experimental knowledge is, however, restricted to the range of high-intensity loads.

Therefore, it can be concluded that there is still a lack of experimental information on the response of cracked concrete to a very large number of load cycles having a relatively low shear stress in relation to the static shear strength.

3 Experimental study

3.1 *Introduction*

From the survey of literature it was concluded that there is still a lack of experimental information with respect to the response of cracks in concrete to "low-intensity high-cycle" loading. Therefore, an experimental study focussing on "low-intensity high-cycle" fatigue of offshore structures was started in the Stevin laboratory.
The first test series was performed with a repeated shear load on pre-cracked reinforced concrete push-off specimens. This type of test represents a shear wall in the basement of an offshore structure. In a substructure placed on the seabed, the static load is generally apparent, and the cyclic load is superimposed on this. For offshore structures, the Arctic and deep sea environments provide intense dynamic forces with a loading frequency of approximately 1 cycle per second [13].
In the second series, the dowel action was eliminated by using external restraint bars, enabling a quantification of the contribution of the aggregate interlock mechanism to the shear transfer. The magnitude of the contribution of the dowel action is then known.
Finally, detailed tests are described in which the axial steel strain in the reinforced push-off specimens was measured during the experiments.
A full survey of all the experimental results has been given in [11, 33].

3.2 *Test arrangement and specimens*

The geometry of the test specimen in this experimental program was similar to the push-off specimen used by Walraven in his static tests [50].
The shear area was 36000 (120×300 mm^2), see Fig. 3.1. Previously, shear tests were performed on specimens with a similar shear area, so the test results can be compared without scale-factors. The specimens were cast in a steel mould placed horizontally, so that at the time of casting the shear plane was in a vertical position. The cantilevers of the specimen were prestressed to prevent preliminary failure of these cantilevers due to secondary cracking. Prior to the actual shear test, the crack was made in a three-point bending test by pushing a steel knife-edge into a V-shaped groove along the shear plane. Both sides of the specimen were subsequently cracked in this manner, resulting in an initial crack width ranging from 0.01 mm to 0.08 mm.
In the reinforced specimens, the normal restraint stiffness was applied by means of stirrups consisting of 8 mm diameter bars crossing the crack plane.
Contrary to this, four external restraint rods were used to apply a normal force on the crack plane of the plain concrete specimens. This force is recorded using strain gauges stuck to the bars.

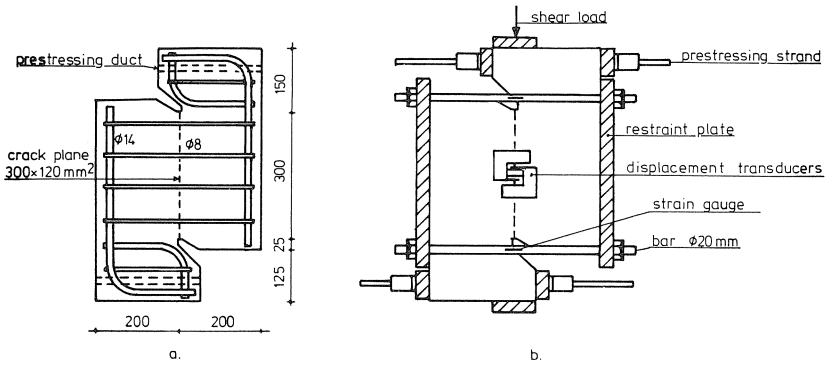

Fig. 3.1. Test specimens used for tests on reinforced concrete (a) and plain concrete (b).

In this case no bars crossed the crack plane. The auxiliary reinforcement was still apparent, preventing preliminary failure of the specimen. Steel plates interconnected by four 20 mm diameter bars were placed at the small sides of the specimen. A thin layer of rapidly hardening sand-cement paste placed between the steel plates and the concrete surface of the specimen ensured an almost linear interaction between crack-opening and restraint force. However, the restraint stiffness remained low compared

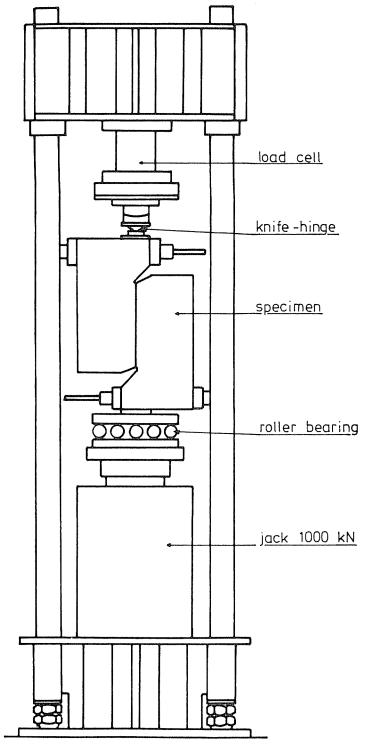

Fig. 3.2. Test arrangement.

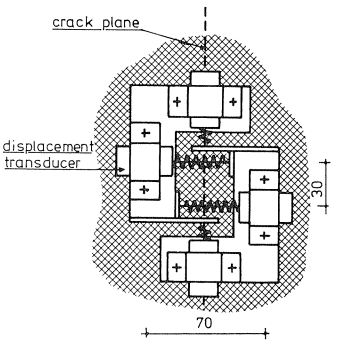

Fig. 3.3. Measuring system.

with the specimens having embedded reinforcement. To ensure a small crack width during the first cycles all the specimens were prestressed with an initial normal stress on the crack plane ranging from 0.8–3.6 MPa.
After pre-cracking, the specimen was centred in the test frame, see Fig. 3.2. The specimen was supported by a roller bearing thus preventing restraining forces from being transmitted during crack opening. The shear load was provided by means of a 1000 kN hydraulic jack placed on the foot of the frame. A knife hinge induced the load at the top of the specimen.
The crack displacements were recorded by means of linear voltage displacement transducers, attached to steel footings glued on the concrete on both sides of the specimen, see Fig. 3.3. The transducers, Hewlett-Packard type 7-DCDT-100, had a 0.01 mm measuring accuracy at 5 mm range.
The shear load was measured by means of a load cell with a measuring accuracy of 0.25 kN. All the signals were fed to a micro-computer for storage and monitor display. In order to reproduce the sinusoidal signals each measured cycle was scanned nine times. A trigger level was adjusted to the maximum load by means of a special circuit. By sampling this trigger level it was possible to start the first scan after each call on the peak value of the applied load.
During the actual test, the specimen was subjected to a shear load, which alternated between a minimum shear stress level τ_0 and a maximum shear stress level τ_m. The crack displacements were not recorded for the first few cycles due to the adjustment of the shear stress levels, the load frequency and the trigger level.

3.3 *Reinforced specimens*

3.3.1 Test variables

The test variables were the reinforcement ratio and steel yield strength, the concrete compressive strength, the initial crack width, the number of cycles and the applied shear stress level.
The normal restraint stiffness depends on the reinforcement ratio ϱ. For the tests, four and six 8 mm diameter stirrups were used, yielding a reinforcement ratio of 1.12% and 1.68% respectively. The steel yield strength of the ribbed bars f_{sy} was 460 MPa (denoted low-strength) and 550 MPa (denoted high-strength) with a rib coefficient f_R (approximately the rib height/rib distance) equal to 0.050 and 0.059 respectively. The use of two steel grades provided an opportunity to investigate whether the reinforcement yielded or not.
The concrete grade f_{ccm} had an average 28-day cube crushing strength of 50 MPa (Mix A) and 70 MPa (Mix B) reflecting the high-strength concrete used in offshore structures.
It can be expected that with increasing concrete strength an increasing number of particles will be fractured during cracking of the concrete, thus reducing the aggregate interlock mechanism. Both mixes had a maximum diameter of 16 mm and almost complied with the Fuller grading curve. Detailed information is given in Appendix I.

The initial crack width varied from 0.01 mm to 0.08 mm to ensure a small crack width (< 0.25 mm) in order to simulate offshore service conditions. For the tests, the initial crack width was not an adjusted, but a measured parameter. The number of cycles ranged from 118 to 931,731 cycles for the test series. The large number of cycles interfered with a good planning of the tests, in general the experiments did not start when the concrete was 28 days old. Therefore, the concrete strength at the start of the test was obtained from Fig. 3.4.

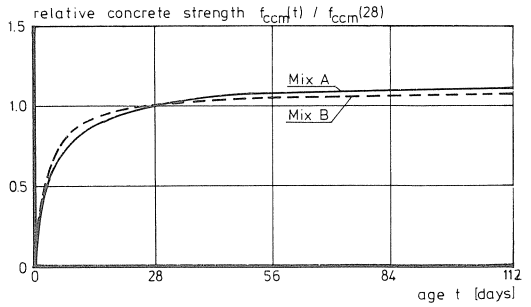

Fig. 3.4. The concrete strength versus the concrete age.

The applied shear stress level is related to the static shear strength obtained in the static tests of Walraven [50]. According to the shear friction analogy, the shear strength can be expressed as a function of the yield strength and the reinforcement ratio [53]:

$$\tau_u = a(\varrho f_{sy})^b \tag{3.1}$$

with

$$a = 0.822 f_{ccm}^{0.406}$$
$$b = 0.159 f_{ccm}^{0.303}$$

During the tests, the shear stress level τ_m was in a range of 46 to 90% of the static strength and a minimum shear stress τ_0 equal to 0.3 MPa. Despite the shear stress of up to 90% of the static strength, the tests were still of the "low-intensity" type because of the very small crack width.

3.3.2 Experimental results

A total of 42 repeated push-off tests were carried out. The specimens were assigned an identifying code consisting of 5 character sets. The first character denotes the concrete grade (Mix A or Mix B), the second the number of 8 mm diameter stirrups and the steel yield strength (Low or High). The next character represents the shear stress level τ_m/τ_u, followed by the actually applied shear stress. Finally, the initial crack width forms part of the identifying code.
Tables 3.1 and 3.2 in Appendix II list a review of the experimental results.

Because of the large number of load cycles, it is hardly possible to show the crack response for each measured cycle. Fig. 3.5 presents a typical relation between the crack displacements in a specific cycle as a function of the shear stress related to the maximum applied shear stress. For this test, a maximum of 1,785 cycles till failure was obtained. Fig. 3.5 shows that even for this relatively small number of cycles the increase in crack displacements between two subsequent cycles remained smaller than the 0.01 mm accuracy of the displacement transducer.

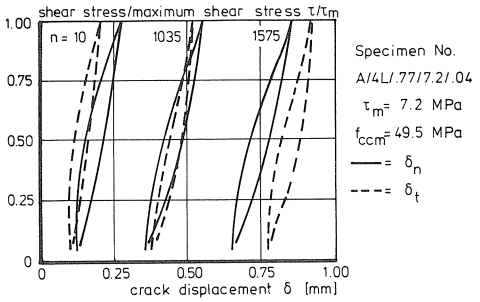

Fig. 3.5. Typical crack response during cycling.

Furthermore, it was observed that the shear displacement increase was initially smaller than the crack width increase, but exceeded the crack width increment with increasing crack displacements.

The influence of the steel yield strength upon the crack response during cycling is shown in Fig. 3.6a, b. The specimens Nos. A/4L/.77/7.2/.04 and A/4H/.78/8.0/.04 were subjected to nearly equal percentages of static shear strength (77% and 78% respectively). Both specimens exhibited a similar behaviour with respect to the crack displacement increase during cycling and followed an identical crack opening path. This indicates that the influence of the steel yield strength can be properly taken into account by equation (3.1) for the static strength. The actual maximum shear stress was

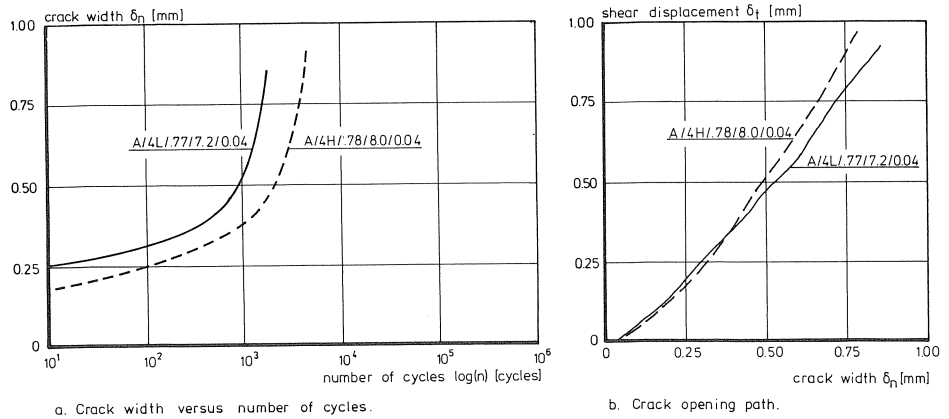

a. Crack width versus number of cycles.

b. Crack opening path.

Fig. 3.6. Influence of the steel yield strength.

7.2 MPa for specimen No. A/4L/.77/7.2/.04 and 8.0 MPa for specimen No. A/4H/.78/8.0/.04 with a calculated static shear strength of 9.38 MPa and 10.26 MPa respectively. Fig. 3.7a, b presents the effect of the variation of the reinforcement ratio. For this parameter it was found that specimens with a different number of bars exhibited a nearly similar response to cycling. The specimens shown in Fig. 3.7, Nos. A/4L/.61/6.1/.03 and A/6L/.61/7.2/0.4, had four and six 8 mm stirrups respectively and were both loaded at 61% of their static strength. Therefore, it can be concluded that the influence of reinforcement ratio is accounted for by equation (3.1).
It is obvious that an increasing concrete strength yields a stiffer crack response to cyclic loading.

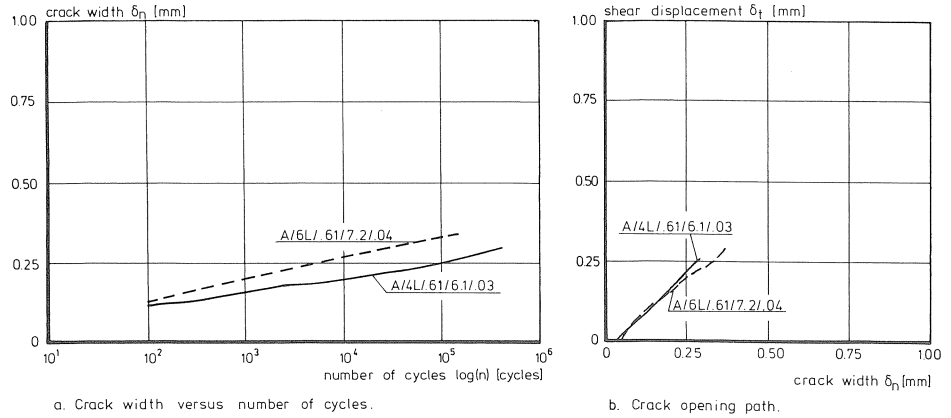

Fig. 3.7. Influence of the reinforcement ratio.

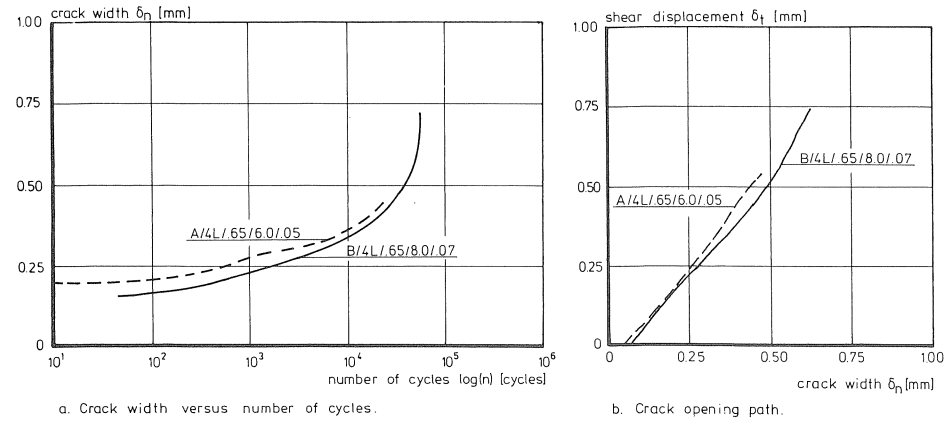

Fig. 3.8. Influence of the concrete grade.

Fig. 3.8a, b shows that the effect of the concrete strength upon this response is also satisfactorily accounted for by the influence of the concrete strength upon the static shear strength. The specimens Nos. A/4L/.65/6.0/.05 and B/4L/.65/8.0/.07 exhibited a similar relation between the crack width and the number of cycles and a similar crack

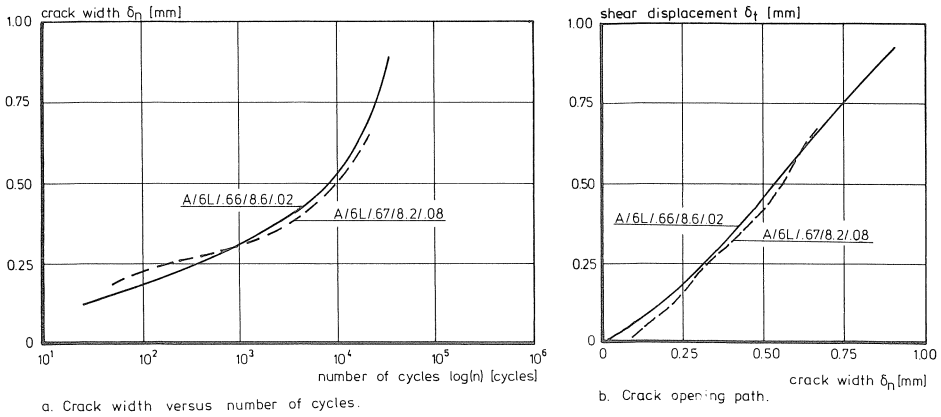

Fig. 3.9. The influence of the initial crack width.

opening path. It must be noted that the relation between the shear displacement and the number of cycles had the same shape as the relation shown in Fig. 3.8a.

Contrary to the previously mentioned parameters, no influence of the magnitude of the initial crack width was found within the range investigated. The specimens Nos. A/6L/.66/8.6/.02 and A/6L/.67/8.2/.08 had a difference in the initial crack width of 0.06 mm. Both specimens followed nearly the same crack opening path except for the small crack displacements.

For mix A, Fig. 3.10a shows the relationship between the crack width and the number of cycles for various shear stress levels. Similar relations were obtained for the shear displacement as a function of the number of cycles, see Fig. 3.10b. The shear stress level is related to the static shear strength according to equation (3.1). Fig. 3.11 presents similar results for mix B.

As expected, the increments of the crack displacements increased with increasing shear stress level. The influence of the parameters investigated in this test series is satisfactorily taken into account by means of the magnitude of the static shear strength. Therefore, the relations presented in Figs. 3.10–3.11 can be approximated by the following empirical expressions, see Fig. 3.12:

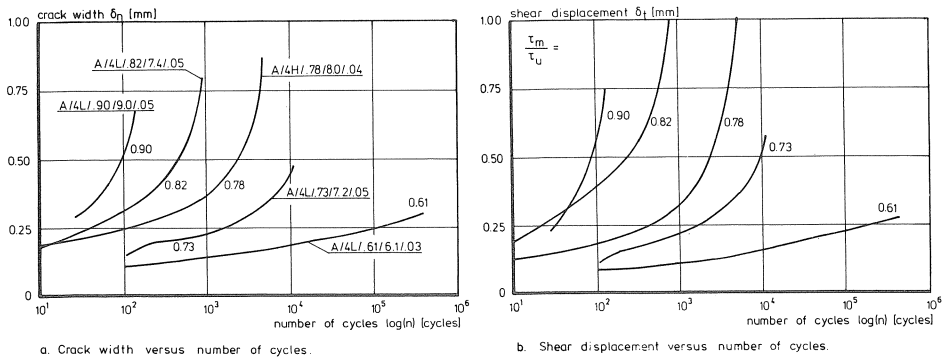

Fig. 3.10. The influence of the applied shear stress level for mix A.

$$\delta_n = 0.10\left(\frac{\tau_m}{\tau_u}\right)^2 + \left[0.15\left(\frac{\tau_m}{\tau_u}\right)^3 + 0.40\left(\frac{\tau_m}{\tau_u}\right)^9\right]\log(n) + 0.20\left(\frac{\tau_m}{\tau_u}\right)^{42}[\log(n)]^{10} \qquad (3.2a)$$

$$\delta_t = 0.10\left(\frac{\tau_m}{\tau_u}\right)^2 + \left[0.07\left(\frac{\tau_m}{\tau_u}\right)^3 + 0.70\left(\frac{\tau_m}{\tau_u}\right)^9\right]\log(n) + 1.17\left(\frac{\tau_m}{\tau_u}\right)^{26}[\log(n)]^5 \qquad (3.2b)$$

with τ_u according to equation (3.1) and δ_n, δ_t in (mm).

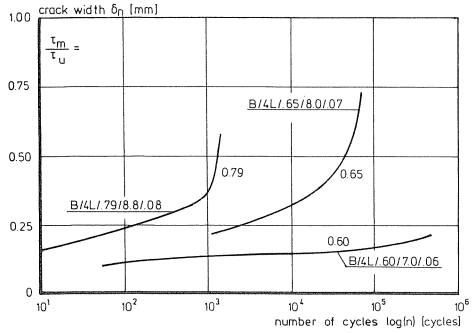

Fig. 3.11. The influence of the applied shear stress level for mix B.

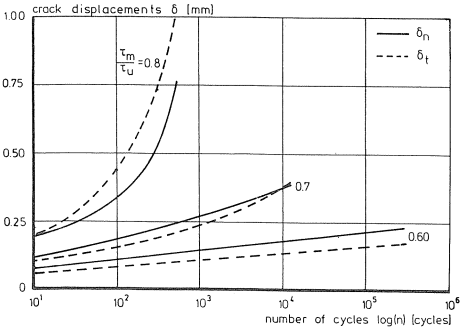

Fig. 3.12. The crack response according to equation (3.2).

In the expressions (3.2) for the crack displacements, the minimum shear stress τ_0 is not apparent. One should assume that the ratio of the applied maximum shear stress τ_m to the applied minimum shear stress τ_0 will strongly influence the relations expressed by equations (3.2a, b).

However, no information on this variable was obtained in this test series.

Fig. 3.13 presents the relationship between the applied shear stress level and the number of cycles till failure. Despite the large scatter, the following mean relation was derived by means of regression analysis:

$$\frac{\tau_m}{\tau_u} = 1.00 - 0.0736\log(n_f) \qquad (3.3)$$

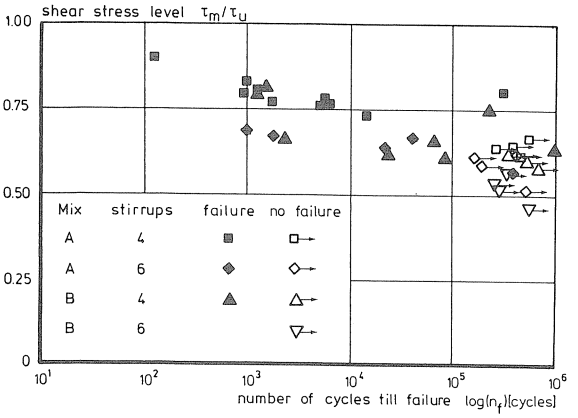

Fig. 3.13. The shear stress level versus the number of cycles till failure.

The specimens which did not fail during cycling were subsequently sheared-off in a static test. Table 3.3 in Appendix II lists the ratio between the shear strength according to equation (3.1) and the experimentally obtained strength. An average ratio of 1.01 with a coefficient of variation of 0.08 was found. Therefore, it can be concluded that preloading with a low shear stress has no measurable influence upon the crack response to higher static shear loads. A similar conclusion can be drawn with respect to higher repeated shear loads. The specimens Nos. B/4L/.57/7.0/.03 and B/6L/.53/8.0/.06 were first loaded to 57 and 53% of their static strength respectively. Both specimens endured more than 250,000 cycles.
Subsequently, they were subjected to a repeated load of 65% of their static strength. Shear failure occurred after 88,500 and 20,632 cycles respectively. These numbers of cycles were in reasonable agreement with the 57,500 cycles according to equation (3.3).

3.4 *Plain concrete specimens*

3.4.1 Test variables

As for the reinforced concrete specimens, the variables used in the experiments with plain concrete specimens were: the concrete grade, the initial crack width, the number of cycles and the applied shear stress level. Instead of the reinforcement ratio for the specimens with embedded bars, the initial normal stress of 0.8–3.6 MPa was now used to ensure very small crack widths. It was found in static push-off tests [50] that for plain concrete no actual failure occurred due to the increasing normal stress. In consequence no shear stress level could be determined related to the static shear strength.
As in the previous experiments, the applied minimum shear stress was 0.3 MPa.

3.4.2 Test results

A total of 14 tests were performed. The identifying code, which was assigned to the specimens consisted of the concrete grade (mix A or mix B), the initial normal stress, the applied maximum shear stress and the initial crack width. Contrary to the experiments on specimens with embedded reinforcement, the applied maximum shear stress τ_m was not the initially applied shear stress. Since no significant crack displacements were recorded for low shear stress levels, the applied shear stress was raised to such a level that significant crack displacements occurred. This stress level was then subsequently maintained and is adopted in the code of the specimen. Table 3.4 in Appendix II lists a review of the experimental results. The experimentally obtained crack response of plain concrete to repeated shear loading is presented in Fig. 3.14.
As for the reinforced specimens, the hysteresic loop indicated that dissipation of energy occurred in the shear plane.
The shear displacement increment was initially smaller than the crack width increment. For increasing crack displacement, the shear slip increment exceeded the increment of the crack width.

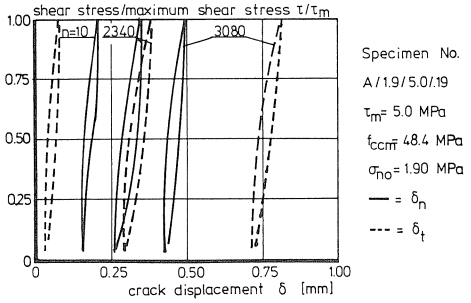

Fig. 3.14. Crack response during cycling.

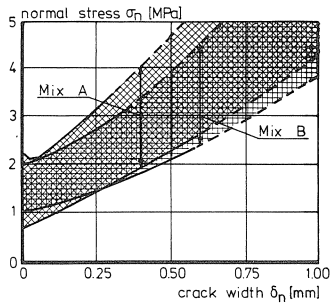

Fig. 3.15. The normal stress versus the crack width.

The specimens were unloaded when the shear displacement was larger than 2 mm. In fact, no shear failure occurred during the repeated tests, because even for large crack displacements ($\delta_t > 2$ mm) the shear plane was still capable of transferring the applied shear load. This was probably due to the increase in normal force with crack-opening. It was found in Walraven's experiments that the static shear strength was proportional to $f_{ccm}^{0.56}$ [50].

For the repeated shear loading tests, the range of the shear stress for which significant crack displacements were recorded was 5.0–6.2 MPa for mix A and 5.6–7.7 MPa for mix B. The average ratio between the range for mix A and the range for mix B was equal to 1.18, which was in good agreement with $(70/51)^{0.56} = 1.19$.

The relationship between the normal stress and the crack width was in the same range for both mixes, see Fig. 3.15. The influence of the magnitude of the initial crack width upon the crack response to repeated shear loading is shown in Fig. 3.16.

The specimens Nos. A/1.3/5.0/.01 and A/1.9/5.0/.19 had an initial crack width equal to 0.01 mm and 0.19 mm respectively.

The last mentioned specimen had a very large crack width during precracking due to a bad fitting of the steel restraint plates to the concrete surface. Although a high normal

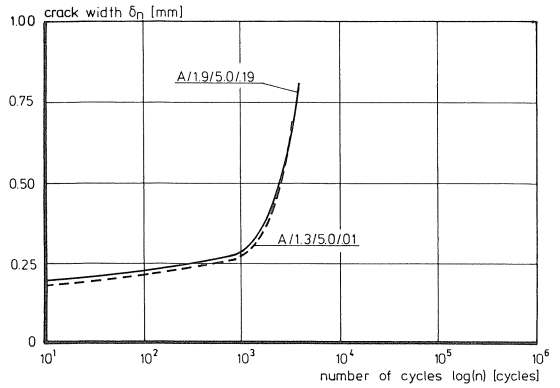

Fig. 3.16. Crack width versus number of cycles as function of the initial crack width.

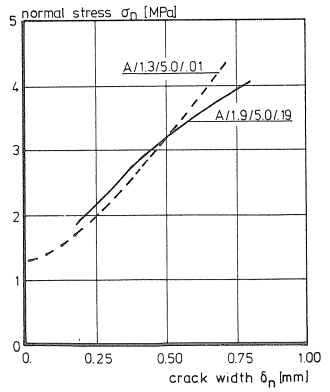

Fig. 3.17. Normal stress versus crack width as function of the initial crack width.

stress was applied to the crack plane, it was not possible to re-close the crack completely. Therefore, this specimen had an initial crack width which was not in the range reflecting offshore conditions.

However, the result is of interest for the influence of the initial crack width. The normal stress as a function of the crack width was similar for both secimens, see Fig. 3.17.

The influence of the normal stress is shown in Fig. 3.18. The specimens Nos. A/0.8/5.5/.01, A/1.3/5.0/.01 and A/2.1/6.1/.01 had initial normal stresses of 0.8 MPa, 1.3 MPa and 2.1 MPa respectively. There was a slight difference in the applied shear stress. Fig. 3.18a shows that the increase in crack width with cycling was similar for both the specimens with the high initial normal stresses. The specimen with the relatively low initial normal stress initially exhibited smaller crack widths, which then increased much more rapidly than for the other specimens.

Obviously, an increase of the initial normal stress up to about 1.3 MPa influenced the crack response. However, a further increase of the normal stress had little effect on the

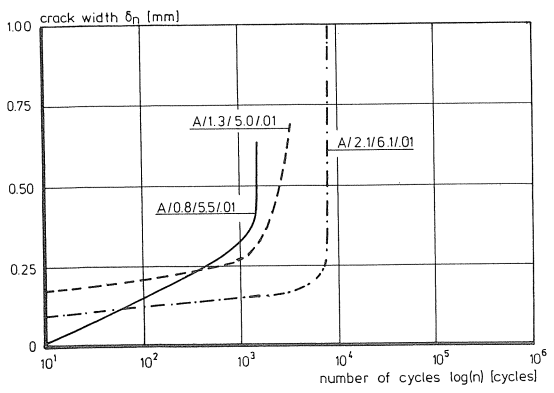

a. Crack width versus number of cycles.

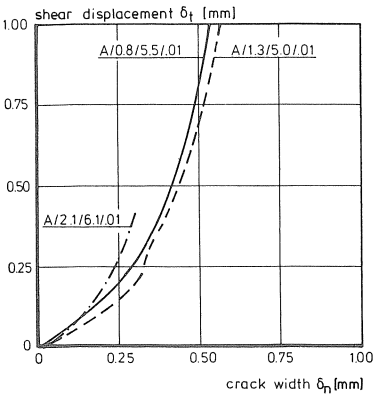

b. Crack opening path.

Fig. 3.18. The influence of the initial normal stress.

increase in crack width. The effect of the normal stress upon the crack opening path was only slight. Fig. 3.18b shows that there was no systematic variation of the crack opening path for the initial normal stress investigated.

The influence of the magnitude of the applied shear stress is shown in Fig. 3.19a, b, representing the crack width versus the number of cycles for both mixes and various shear stresses. Contrary to the specimens with embedded reinforcing bars, the increase in crack displacements appeared to be hardly affected by the applied shear stress. An exception was obtained for the specimen with the relatively low initial normal stress of 0.8 MPa, as has already been shown in Fig. 3.18.

Shear failure occurred when the crack faces became unable to transfer the applied shear stress and was characterized by an abrupt increase in the crack displacements, instead of the gradual increase observed for the reinforced specimens. The crack opening paths for mix A varied only within a small range, see Fig. 3.20a. For mix B, a somewhat wider range was found, with a crack opening path which deviated slightly from the mean crack opening path of mix A, see Fig. 3.20b.

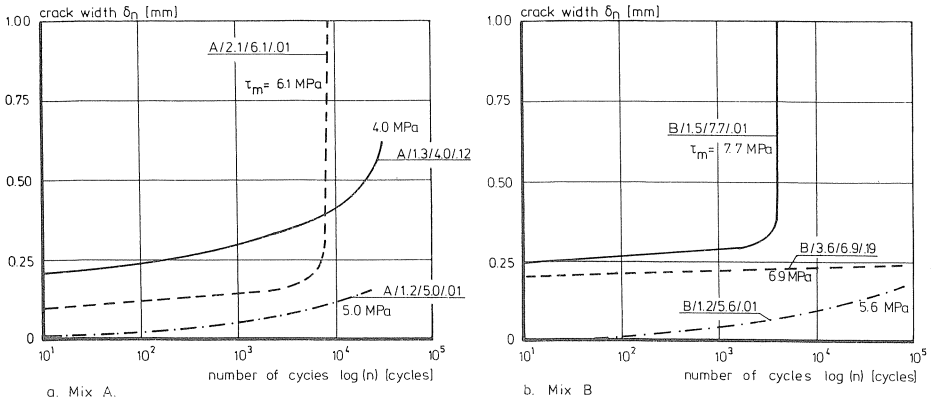

Fig. 3.19. The influence of the applied maximum shear stress.

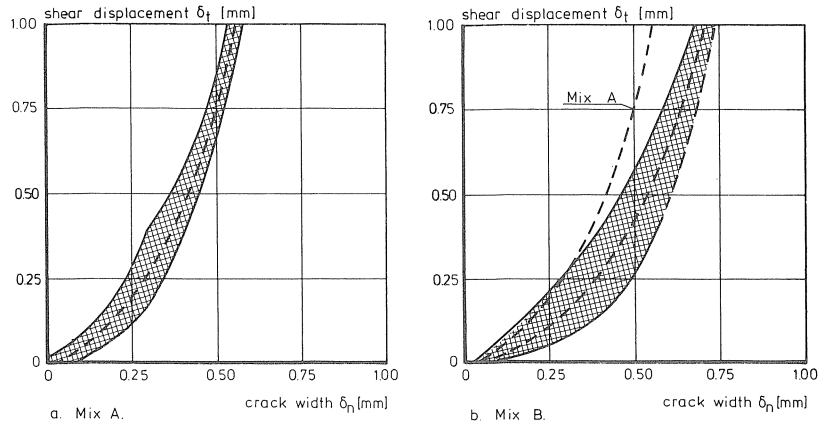

Fig. 3.20. Crack opening paths for both mixes.

The number of cycles till failure was not only influenced by the applied shear stress, but also by the normal stress. Although no ultimate shear stress is clearly defined for experiments with an increasing normal stress, a rough approximation of the static shear strength can be made using the experimental results of Walraven [50] and Daschner [5]. Daschner's results were questionable [6] with respect to the measured crack displacements, but the relation between the (constant) normal stress and the static shear strength was properly recorded, see Fig. 3.21. The following expression for the static shear strength was derived by means of a regression analysis [51]:

$$\tau_u = 1.647 f_{ccm}^{0.321} \sigma_n^{0.427} \tag{3.4}$$

For the present test series, the normal stress at the onset of shear failure was presented in [33]. Inserting this value of the normal stress into equation (3.4), the number of cycles till failure is related to the (approximated) shear stress level, see Fig. 3.22. Despite the scatter of the results, it appeared that most of the plain concrete specimens endured less cycles than the reinforced specimens at the same shear stress level. In Fig. 3.22 this is shown by means of the broken line according to equation (3.3).

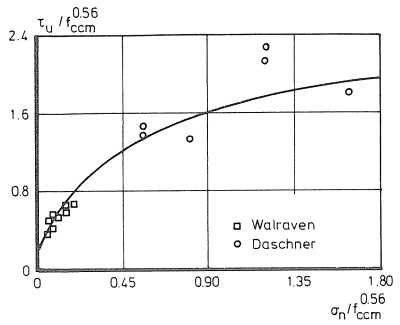

Fig. 3.21. Shear strength versus normal stress [51].

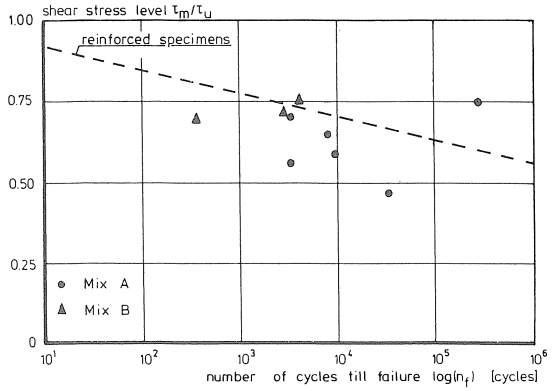

Fig. 3.22. Shear stress level versus number of cycles till failure.

3.5 *Additional detailed tests*

The major disadvantage of push-off tests with reinforced specimens was that the normal stress on the crack plane could not be measured. The test series with plain concrete specimens only partially solved that problem. It appeared from the experimental results that the crack opening direction of the specimens differed from the crack opening path of the plain concrete specimens, thus yielding a different crack response to cycling.

Therefore, additional detailed tests were performed to study the normal stress-crack width relation for reinforced specimens. The specimen geometry and the test procedure were the same as used in the main test series. However, the steel strain of the

reinforcing bars was in this case recorded by means of a bolt gauge, type BTM-8 of Tokyo Sokki Kenkyojo. These tests are fully described in [11].
Half of all the bars crossing the crack plane were prepared with a bolt gauge, which was cemented at the neutral axis near the crack plane, see Fig. 3.23.

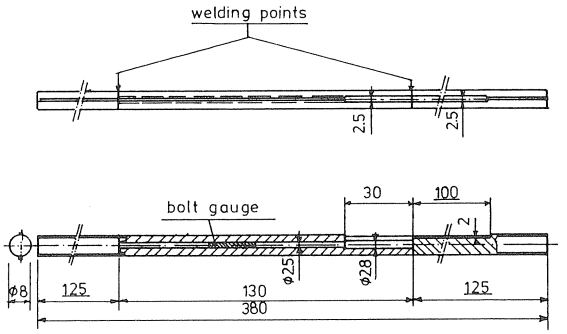

Fig. 3.23. Bar prepared with bolt gauge.

The overall dimensions of the gauge were 20 mm × 2 mm with a working length of 8 mm × 1 mm [43].
The normal force was measured with an accuracy of 0.1 kN for 8 mm diameter bars or 0.2 kN for 12 mm diameter bars. This type of bolt gauge was chosen so as to prevent changes of the bond characteristics of the bar close to the crack plane. In order to position the gauge at the centre line of the bar a 2.5 mm diameter hole was drilled resulting in a reduction of the cross-sectional area of approximately 10% for the 8 mm bars. The hole was 130 mm long, which was the maximum to be achieved by drilling from both sides. This length was important because of the attachment of the wires to the bar, which must be situated as far as possible from crack plane.
Therefore a small piece with a length of 130 mm was sawn out of the original stirrup, prepared and replaced by means of an electric welding and upsetting machine. Special care was taken to obviate the influence of the welding heat upon the material properties of the steel.
Finally, the bolt gauge was glued in the hole using polyester resin adhesive. A series of preliminary tests was performed to investigate the actual characteristics of the prepared bars.
First a tensile test on the bare bar was carried out to determine the stress-strain relation of the prepared bar. At a steel stress of 240 MPa brittle fracture of the weld occurred. All prepared bars were then preloaded up to 160 MPa in order to derive the actual stress-strain relation, see Fig. 3.24a.
Second, a pull-out test was performed.
The steel strain was measured by means of a bolt gauge glued at the centre line of the bar, which was positioned at a distance of 50 mm from the bearing plate of the pull-out specimen. This relation is shown in Fig. 3.24b, for a 8 mm bar and a concrete strength of

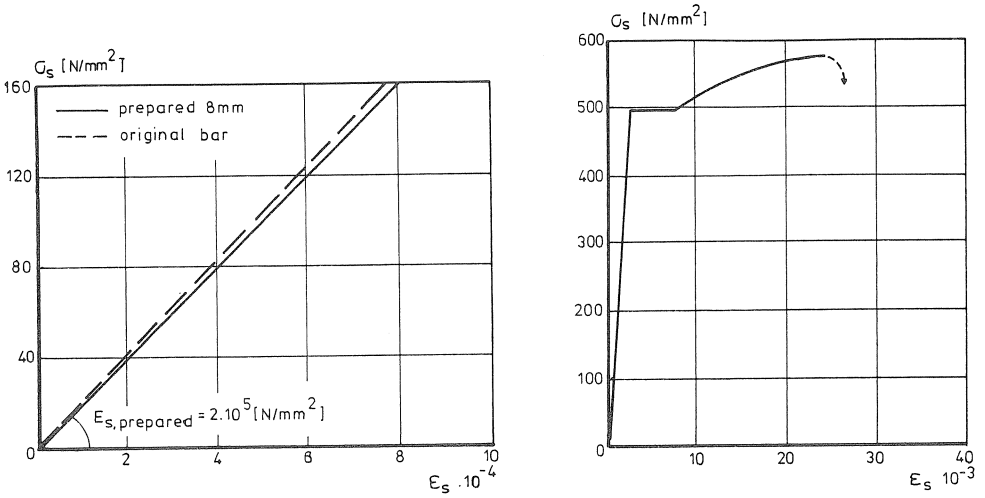

Fig. 3.24. Preliminary tests with prepared bars.

approximately 40 MPa. The bond length used was rather long, 90 mm. Due to this transmission length the bar yielded before pulling-out.
A total of six push-off tests was performed.
Three series of two specimens were subjected to static, sustained and repeated shear loading. The results of the static shear loading tests will be described here.
For the static loading tests, the concrete cube strength was approximately 50 MPa. The parameter investigated in these tests was the bar diameter. Specimen No. D1 was reinforced with eight 8 mm diameter bars, while specimen No. D6 had three stirrups consisting of deformed 12 mm diameter bars. Some experimental results are shown in Fig. 3.25.

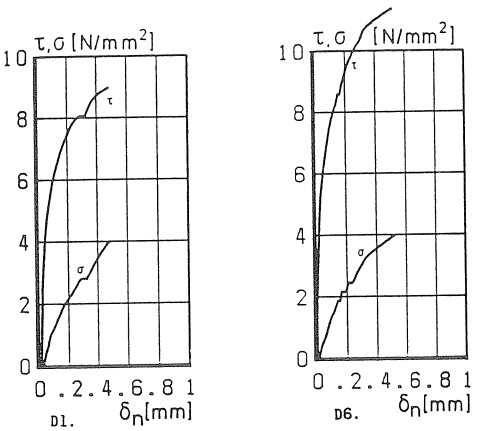

Fig. 3.25. Experimental results of the static shear loading tests.

4 Theoretical analyses of the response of cracked concrete to shear loading

4.1 *Introduction*

Physical models properly describing the mechanisms of aggregate interlock and dowel action are derived for the case of increasing shear loads [12, 35, 50]. These models will be briefly discussed and their presentation will be adapted to the case of constant shear loads.
Furthermore, newly observed material behaviour is incorporated in these models.
In the case of cycling shear loading, a distinction is made between the description of "high-intensity low-cycle" fatigue on the one hand and "low-intensity high-cycle" fatigue on the other hand. The existing static models will be adapted in line with the situation of cycling loading. On the basis of the basic transfer mechanisms, the cyclic shear transfer in cracked reinforced concrete will be discussed.

4.2 *The aggregate interlock mechanism*

Walraven [50] developed a physical model, based upon the assumption that concrete can be conceived as a composition of two basically different materials; the strong and stiff glacial river aggregate particles and the matrix material consisting of hardened cement paste with a much lower strength and stiffness. If a crack is formed in the concrete, it will run through the matrix material and along the interface of the matrix and the particles. Therefore, the crack plane exhibits a global ondulation caused by the irregular shape of the crack faces and a local roughness due to the particles protruding from the crack plane. The crack plane can therefore be approximated by a flat plane intersected by stiff particles. Next, the irregularly shaped particles are randomly orientated. The most accurate simplification of the particles according to Walraven's assumptions is shown in Fig. 4.1.
His schematic two-phase presentation of the actual crack plane provides a physically close approximation of the experimentally observed crack response to static shear loads. The particles are regarded as rigid spheres embedded in the matrix material, which is considered as a rigid material with crushing strength σ_{pu}. In consequence, the particles are undeformably crushing the matrix during shear sliding.

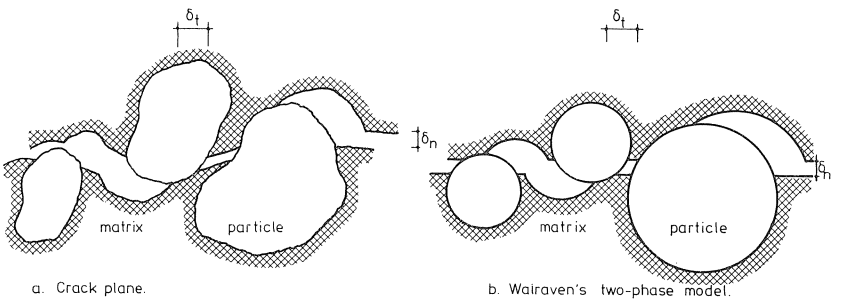

Fig. 4.1. Crack plane according to Walraven's two-phase model [50].

Whether a particle makes contact with the opposing crack face depends upon the particle size, its embedment depth, the crack width and the shear displacement. An interesting aspect of Walraven's schematic presentation of the crack plane is that the total contact area of all the particles in a unit area of the crack plane can be determined analytically. Considering a gradation according to Fuller's ideal curve, Walraven quantified the projected contact areas a_x and a_y for any given particle during shear sliding, see Fig. 4.2a. For a thin slice of the crack plane the particles reduce to circles, whose occurrence in the crack plane is described by a probability density function. The projected contact areas in this thin slice can be determined analytically as the distance between the intersection point of two circles and the intersection point of a straight line and a circle. All the projected contact areas a_x and a_y are summed up numerically yielding the total projected contact areas A_x and A_y for unit area of the crack plane. Now, the equilibrium condition for this unit area can be described by, see Fig. 4.2b:

$$\tau_a = \sigma_{pu}(A_y + \mu A_x) \tag{4.1a}$$

$$\sigma_a = \sigma_{pu}(A_x - \mu A_y) \tag{4.1b}$$

in which

τ_a = shear stress
σ_a = normal stress
σ_{pu} = strength of matrix material
A_x = total projected contact area per unit area of the crack plane parallel to the crack plane
A_y = total projected contact area per unit area of the crack plane normal to the crack plane

The strength of the matrix material σ_{pu} and the coefficient of friction were derived from the experimental results of Walraven's static tests [50]:

$$\sigma_{pu} = 6.39 f_{ccm}^{0.56} \tag{4.1c}$$

$$\mu = 0.4 \tag{4.1d}$$

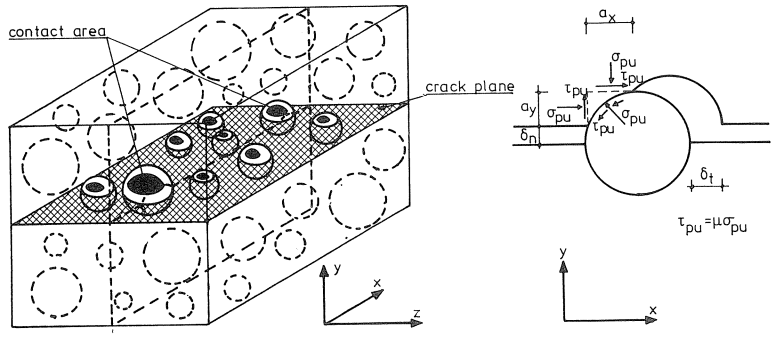

Fig. 4.2. Contact area during shear sliding.

Fig. 4.3 presents a comparison of the model with some typical test results [50]. Apart from his own experimental results, Walraven's model provides good predictions for tests by Paulay et al. [31] and Millard et al. [26].

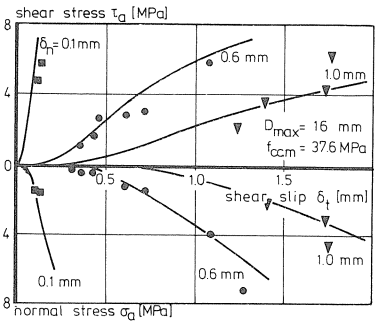

Fig. 4.3. Comparison of the model with experimental results [50].

The two-phase model as presented in Fig. 4.3 describes a unique relationship between the stresses and the displacements in the crack plane.
For the purposes of this paper, it was preferred to present this relationship as crack opening paths for constant shear or constant normal stresses.
These stresses are related for the matrix strength according to equation (4.1c), see Fig. 4.4a, b.
According to the model the maximum particle size has a slight influence upon the crack response. This is shown in Fig. 4.4 for particle diameters of 10 mm, 16 mm and 32 mm. The lower the size of the maximum particle the steeper the crack opening path (δ_t-increment > δ_n-increment). For this particular case, the determination of the contact areas according to Walraven's model is too complex. Therefore, empirical relations are derived which satisfactorily describe the relationship between the contact areas and the crack displacements.

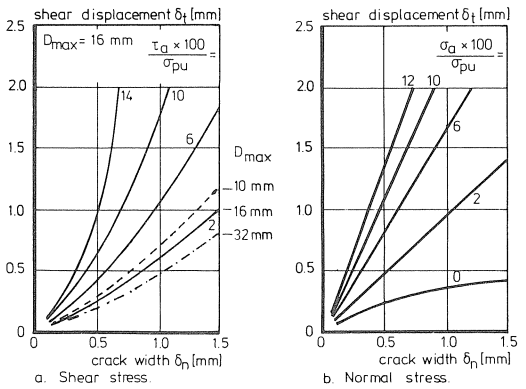

Fig. 4.4. Crack opening path according to the model.

$$A = \frac{p_k}{75}\left(a\,\frac{K - 1 + \exp(-K)}{\exp(-K)/K + 1} + b \cdot p\right) \qquad [\mathrm{mm^2/mm^2}] \tag{4.2a}$$

with

$$K = b/a \cdot \delta_t \tag{4.2b}$$

for A_x: $a = 4$ (4.2c)

$$b = 7.00 D_{max}^{0.056}\,\delta_n^{-1.07} \tag{4.2d}$$

$$p = 0 \tag{4.2e}$$

for A_y: $a = 2$ (4.2f)

$$b = 3.00 D_{max}^{0.280}\,\delta_n^{m} \tag{4.2g}$$

$$m = -1.47 D_{max}^{-0.063} \tag{4.2h}$$

$$p = 0.5([\delta_n - \delta_t] - \mathrm{abs}\,[\delta_n - \delta_t]) \cdot \exp(-1 - D_{max}/32 - 0.5\delta_n^2) \tag{4.2i}$$

The limitations of the equations are:
- $\delta_t < 1.2\delta_n$;
- Particle distribution according to Fuller.

In the case of settlements, large shear displacements can occur. In that case the original formulas of the two-phase model must be used.
In the case of the cracked plain concrete subjected to cyclic or repeated shear loading, a distinction is made between "high-intensity low-cycle" fatigue.
This distinction is made for practical reasons as it appeared from the low-intensity experiments described in Chapter 3 that the crack displacement increments per cycle can be less than the numerical accuracy of any mathematical model. Therefore, the response of a cracked element to this type of cyclic loading must be described by the over-all degradation and the irreversible deformations of the concrete due to cycling. Subsequent cycles with a very high amplitude can be described by the model for "high-intensity low-cycle" fatigue. For this type of fatigue, Walraven gave a qualitative description the crack response in plain concrete to cyclic shear loading [50], (1980). He derived the following expression for the reduction in shear stress before any displacement backwards can occur during unloading the specimen:

$$\frac{\tau}{\tau_m} = \frac{A_x - \mu A_y}{A_x + \mu A_y}\,\frac{A_y - \mu A_x}{A_y + \mu A_x} \tag{4.3}$$

This expression is based upon the two-phase model, which predicted a crack response as shown in Fig. 4.5.
During re-loading in the second or any subsequent cycle, the shear displacement can increase without (hardly) any shear load. This free slip is caused by the already deformed matrix material. A further increase in the shear load brings the particle firmly into contact with the matrix material. However, the contact area cannot be calculated according to the analytical two-phase model.

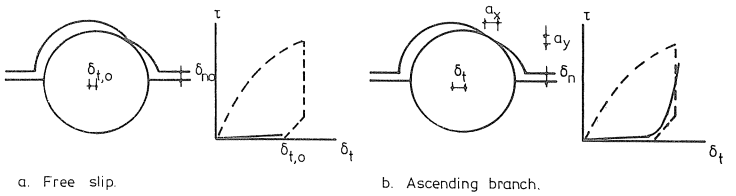

Fig. 4.5. Qualitative description of the response to cyclic shear loads.

Walraven modified the calculation of the contact areas of the particles (1986, [52]) by replacing the analytical solution by a numerical solution. In this the shape of the contact area of each particle in the crack plane is monitored by means of several points situated on the surface of the deformed matrix material, see Fig. 4.6.

For a specific combination of the crack displacements, it is possible to determine the highest and the lowest points which are situated in the contact area. Now, the projected contact areas a_x and a_y can be determined as the distance between those points in parallel and normal direction respectively. Taking into account several particle diameters and embedment depths, the total contact areas per unit area of the crack plane A_x and A_y can be calculated as in the original analytical two-phase model. Again, the presence of a specific particle is accounted for by a probability density function [50].

This modification of the two-phase model will be referred to here as the numerical contact model.

With this model, Walraven simulated the cyclic push-off tests of Laible [19, 20]. The particles used in this test series had a moderate strength. Consequently, the number of particles fractured during cracking of the concrete was large in relation to the number of fractured glacial river particles used by Walraven. Hence, a reduction of the total contact areas must be taken into account.

Furthermore, the coefficient of friction must be adjusted to the proper value for this type of aggregate.

From the experimental results of the first cycle of the test, Walraven derived a reduction factor of 0.75 and a coefficient of friction equal to 0.20.

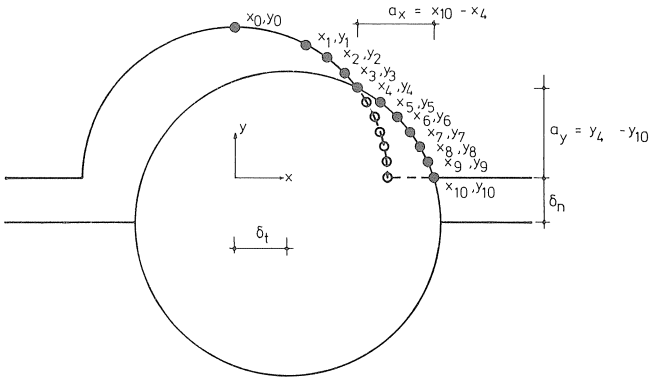

Fig. 4.6. Representation of the contact area by means of points situated in the contact area [52].

After these values had been inserted into the model, the subsequent cycles were simulated, see Fig. 4.7.
For reasons of symmetry, only the results of the positive direction and shown. A good agreement between the experimental and the calculated results is found. It appeared from the calculation that no reduction of the matrix strength due to cycling has to be taken into account. This is probably due to the fact that the high contact stresses are only apparent in the contact areas. In Laible's tests, the displacement increments in each cycle are large enough to crush the previously loaded matrix material and subsequently to load new material.

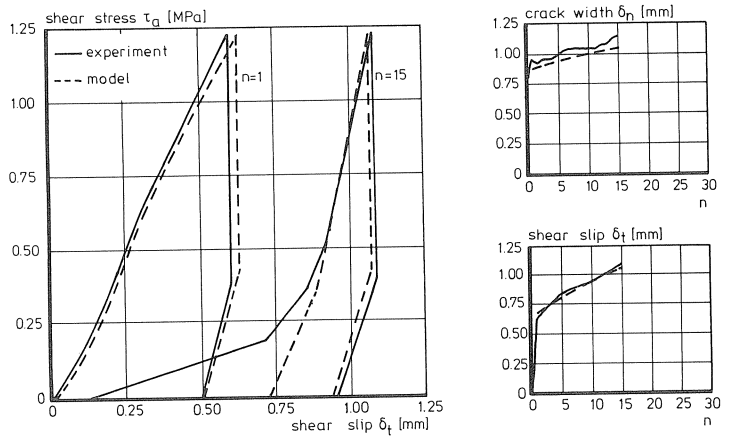

Fig. 4.7. Comparison of the experimental result of test No. A1 of Laible with the numerical contact model [52].

The experimentally obtained normal restraint stiffness served as input data for the program. Walraven demonstrated that the numerical contact model is suitable for describing the crack response to cyclic and repeated shear loads. This model can be used to perform sensitivity studies, but is too complex for implementation in advanced finite element programs. Although the numerical contact model developed by Walraven is suitable for all loading types, its major disadvantage is that all cycles have to be taken into account. For practical use, the physical model must describe the over-all response degradation and the irreversible deformations due to "low-intensity" load cycles. Therefore, it s assumed that the load history is fully incorporated in the contact areas which are formed in the last load step of the previous cycle. This assumption is shown in Fig. 4.8.
An important conclusion resulting from this assumption is that it holds true for all the intermediate load steps in a cycle. Then the magnitude of the contact area can be determined analytically by means of the intersection points of three circles. With this model, referred to as the analytical contact model, test No. A1 of Laible [19] was simulated using ten particle diameters and ten embedment depths, see Fig. 4.9.

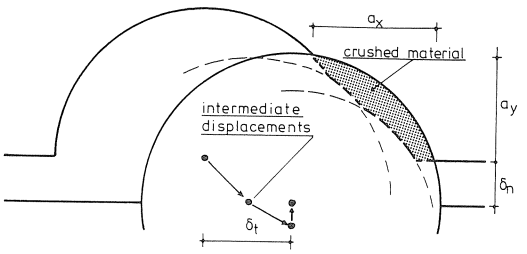

Fig. 4.8. The load history incorporated in the end-deformation of the crack plane.

Input in the program was the end displacement of the first load cycle. Therefore, the first cycle was not simulated. It appeared that the crack response is satisfactorily described even if the three pairs of coordinates of the three circles remain the same for all particle diameters. Therefore, six coordinates determine the total contact areas in normal and parallel direction.
A further simplification can be obtained by reducing the number of particle diameters and embedment depths.
There is, however, an even simpler method. During cycling, the stresses in the crack plane for a given combination of the crack displacements are as large as or less than in the case of a static test. This is due to the reduced size of the contact areas, thus:

$$\tau_a = \sigma_{pu}(\lambda_y A_y + \mu\lambda_x A_x) \tag{4.4}$$

$$\sigma_a = \sigma_{pu}(\lambda_x A_x - \mu\lambda_y A_y) \tag{4.5}$$

with

A_x, A_y = total contact areas for the static case
λ_x, λ_y = reduction factors

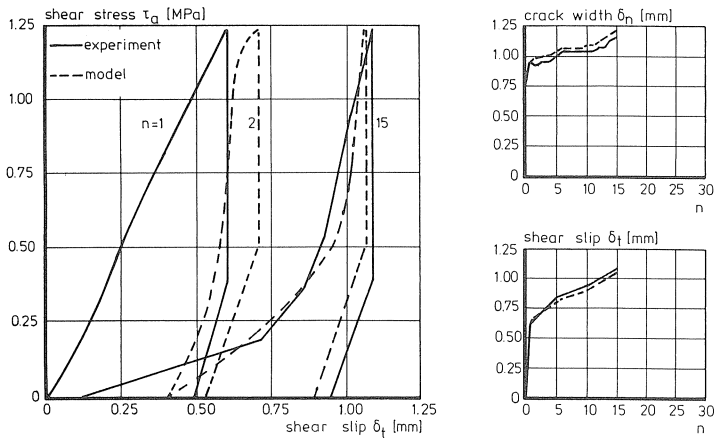

Fig. 4.9. Comparison of the experimental result of test No. A1 of Laible with the analytical contact model.

For test No. A1, these reduction factors are derived on the basis of the calculation process using the analytical contact model, see Fig. 4.10. It appeared that these factors can be approxomated by:

$$\lambda_x = 0.8 \left(\frac{\delta_t - \delta_0}{\delta_{tm} - \delta_0} \right)^2 \tag{4.6}$$

$$\lambda_y = 0.7 \left(\frac{\delta_t - \delta_0}{\delta_{tm} - \delta_0} \right)^3 \tag{4.7}$$

with

$\delta_0 \quad = \delta_{nm} - \sqrt{\delta_{nm}^2 - \delta_{no}^2} < 0.67\delta_{tm}$
$\delta_{nm}, \delta_{tm} =$ end displacement of previous cycle
$\delta_{no} \quad =$ initial crack width

With equations (4.6–4.7), the calculation process becomes quasi-static.

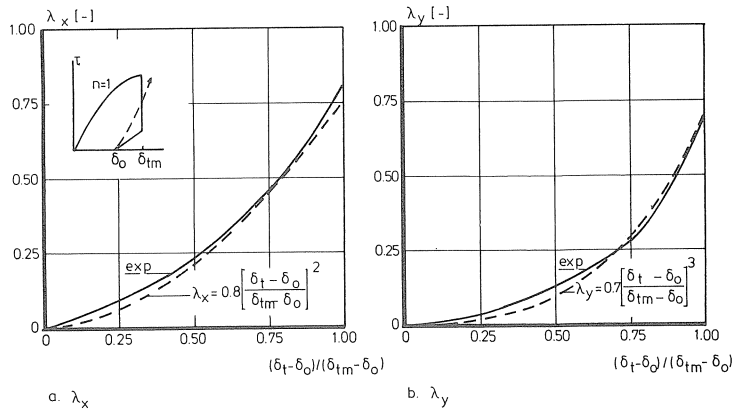

Fig. 4.10. The contact area reduction factors.

Substitution of equations (4.2a–i) in the model yields a simple version of the model, which is referred to as the reduced contact model. The calculated response of test No. A1 shows a good agreement with the exerimental results, see Fig. 4.11.
Equations (4.6–4.7) are derived on the basis of the results of Laible's test No. A1 of Laible. Fig. 4.12 shows that the reduced contact model also provides good predictions of tests with smaller crack widths and higher normal restraint stiffnesses.
In Fig. 4.13 the results of test No. E1 of Laible are shown. In this test, twenty load cycles with a maximum shear stress up to 0.69 MPa were applied to the specimen, followed by five cycles with a maximum shear stress of 1.24 MPa. Because of the assumption that the end deformation of the contact areas incorporates the load history, only the cycles Nos. 21 to 25 are simulated. Although the calculated crack response is somewhat too stiff, the over-all behaviour is satisfactorily predicted. It must be noted, however, that

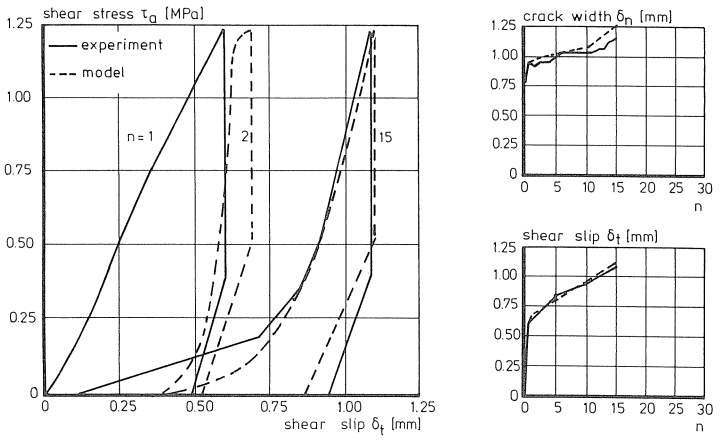

Fig. 4.11. Comparison of the experimental result of test No. A1 of Laible with the reduced contact model.

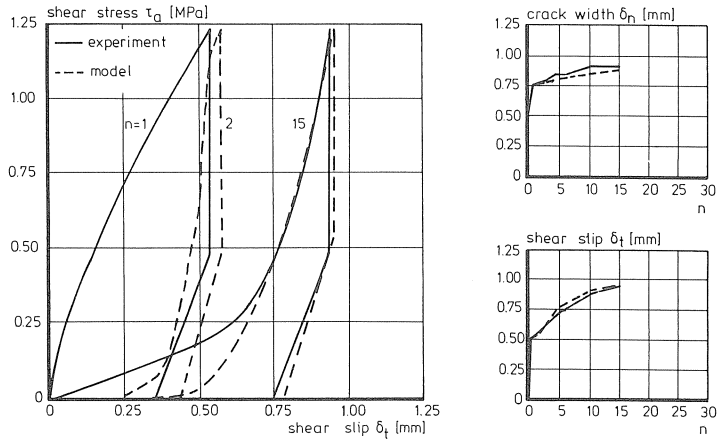

Fig. 4.12. Comparison of the experimental result of test No. C1 of Laible with the reduced contact model ($\delta_{no} = 0.51$ mm).

both the analytical and the reduced contact model are only valid for load cycles in which the maximum shear stress is at least equal to the maximum shear stress in any previous cycle.

Simulating the above-mentioned shear tests, it emerged from the calculation that there was no decrease in matrix strength due to cycling. This is probably due to the fact that the crack displacement increments are relatively large in the case of "high intensity" fatigue.

The high stresses causing fatigue of the matrix material are restricted to the volume close to the contact areas. Due to the increasing displacements, the previously loaded

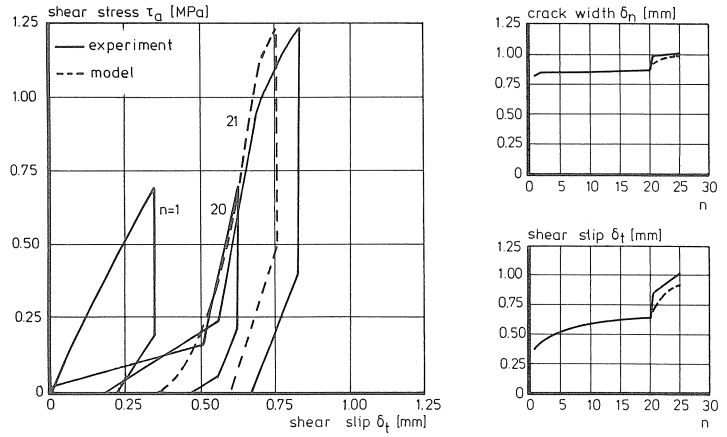

Fig. 4.13. Comparison of the experimental result of test No. E1 of Laible with the reduced contact model ($\delta_{no}=0.76$ mm).

matrix material is crushed and the matrix material lying behind is then subjected to high contact stresses. This matrix material was subjected to low stresses in the previous cycles, so no fatigue of the material has occurred. In the case of "low-intensity high-cycle" fatigue, the crack response can theoretically be simulated with the proposed models. If the initial crack width is reduced to 0.15 mm and a normal restraint stiffness of 7.5 MPa/mm is used, a shear stress of 3 MPa can be transferred by the crack plane.
The crack displacement increase in each cycle rapidly diminishes until it becomes smaller than the numerical accuracy, indicating that the actual displacement increase is even smaller. In this case the crack displacement increments are very small, so a reduction of the matrix strength now occurs due to cycling.
On the other hand, "high-cycle" tests are generally performed with a rather high loading frequency, which might cause rate effects and thus increases the matrix strength. Because of the small displacement increment, the fatigue of the suggested matrix material and the rate effects, empirical expressions must be used to describe the increase in crack displacements due to "low-intensity" cycles.

4.3 *The mechanism of dowel action*

The mechanism of dowel action is based upon the response of a bar and the surrounding concrete to a lateral bar displacement. As described in Section 2.3, failure of a dowel occurs due to crushing of the concrete and yielding of the bar when the concrete cover of the bar is sufficient large to prevent splitting failure.
In the case of crushing failure three mechanisms can be distinguished, according to Paulay [32]:

a. bending; the dowel force is transmitted due to bending of the bar. For this mechanism the ultimate load is reached due to yielding of the bar;

b. pure shear; it is expected that the transfer of dowel force by means of pure shear is unlikely because of the deterioration of the concrete in the vicinity of the bar. Therefore, the resulting dowel forces at both sides of the crack plane have a relatively large eccentricity resulting in yielding of the bar due to bending;
c. kinking; for a considerable lateral bar displacement the axial bar force in the crack plane has a component parallel to the crack direction. In the case of cracked concrete the crack width remains small relative to the bar diameter. Hence, the effect of kinking of the bar will be small (except for the case of large crack widths in combination with small bar diameters).

The dowel load-lateral displacement relation can be described using the theory of beams on elastic foundation, as published by Timoshenko and Lessels [42]. Now the bar is considered as a flexible beam of infinite length supported on an elastic foundation. This mechanism was first used by Friberg [12] and accounts for the bar diameter and the concrete strength. According to this mechanism, the following relation can be derived:

$$\delta_t = F_d \frac{1}{2\beta^3 EI} \qquad \text{[mm]} \tag{4.8}$$

with

$$\beta = \sqrt[4]{\frac{K_f \phi}{4EI}}$$

K_f = foundation modulus of concrete [MPa/mm]
ϕ in [mm], E in [MPa], I in [mm]

According to experimental observations [32], the foundation modulus is not a material constant, but decreases with increasing lateral bar displacement, see Fig. 4.14.
The beam on elastic foundation theory provides a good prediction of the dowel load-lateral bar displacement relation up to a dowel force of approximately 50% of the dowel strength. With increasing dowel force the concrete stresses in the vicinity of the bar exceed the uniaxial compressive strength. However, the surrounding concrete provides

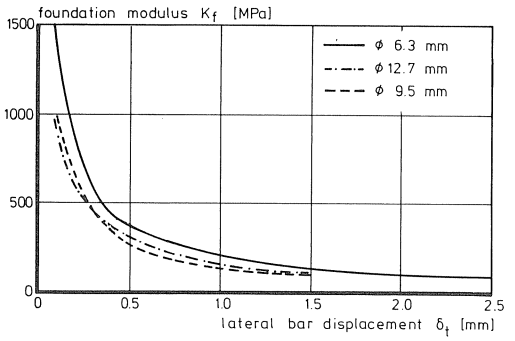

Fig. 4.14. Foundation modulus as function of the lateral bar displacement [32].

a considerable confining pressure, thus yielding a triaxial compressive zone under the bar. Therefore, the concrete strength may be several times as high as the uniaxial strength. Now, the bar itself becomes the weakest link and the ultimate dowel force is reached when the bar yields. Rasmussen [35] performed tests on dowels protruding from a large concrete block, see Section 2.3. Apart from his experimental study, Rasmussen modelled the dowel action according to the behaviour of the steel dowels in timber structures. Fig. 4.15 presents the failure mechanism in which a plastic hinge is situated at some distance from the "crack plane". In the plastic hinge the plastic moment of the bar is reached, which is equal to $0.167 f_{sy} \phi^3$.
Now, the equilibrium condition yields:

$$F_d = B\phi^2 \sqrt{f_{ccyl} f_{sy}} \quad [N] \tag{4.9a}$$

with

$$B = C\left(\sqrt{1 + [\varepsilon C]^2} - \varepsilon C\right) \tag{4.9b}$$

$$\varepsilon = 3\,\frac{e}{\phi}\sqrt{\frac{f_{ccyl}}{f_{sy}}} \tag{4.9c}$$

e = eccentricity of the dowel load (mm)
C = empirical constant

It was found experimentally that C was equal to 1.3, assuming a zero-eccentricity of the dowel load.
Similar expressions are derived by Dulacska [8] and Vintzeleou [48].
Rasmussen's failure mechanism accounts for the reduced reaction stresses in the vicinity of the crack plane as observed experimentally by Dulacska [8] and Utescher [45]. Equation (4.9) provides a good prediction of experimentally obtained dowel

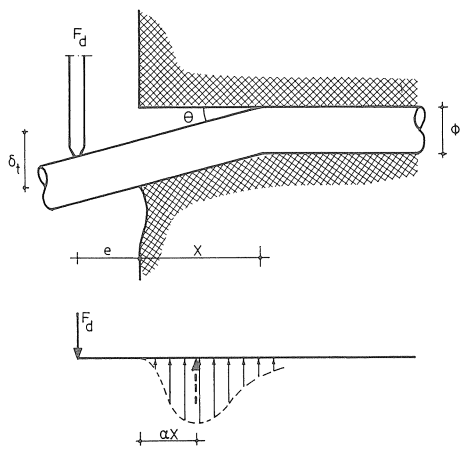

Fig. 4.15. Failure mechanism according to Rasmussen [35].

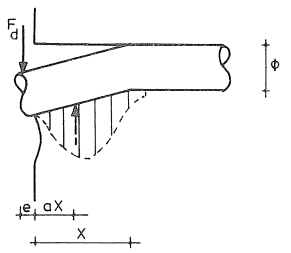

Fig. 4.16. Failure mechanism of bar due to plastification.

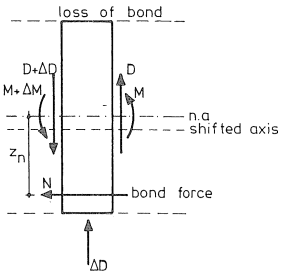

Fig. 4.17. The equilibrium condition for the plastic hinge.

strengths, although the calculated dowel strength is somewhat too low for very small load eccentricities. Because of its good over-all description of the dowel strength, Rasmussen's model will be used here for a further analysis of the dowel failure mechanism.

Fig. 4.16 presents a bar protruding perpendicularly from a concrete block. At a distance X from the "crack plane" a plastic hinge had been developed. The magnitude and the distribution of the reaction stresses in the concrete under the bar are not known beforehand. According to the theory of plasticity the plastic moment of the bar is equal to $0.166\phi^3 f_{sy}$. However, this plastic moment can only be applied to a bare bar. In the case of a dowel embedded in concrete, the concrete supporting the bar in the cross-section situated at the plastic hinge of the bar is deformed due to the lateral bar displacement. In consequence, the bond between the bar and the concrete above the bar must be broken. Contrary to this, the bond between the bar and the concrete supporting the bar will be extremely good due to the high reaction stresses. For the cross-section in which the plastic hinge is situated, the equilibrium condition is shown in Fig. 4.17. The resulting force due to the bond stresses between the bar and the concrete supporting the bar is situated at a distance z_n from the neutral axis of the bar.

Due to the bond force the neutral axis of the bar is shifted over a distance z, see Fig. 4.18.

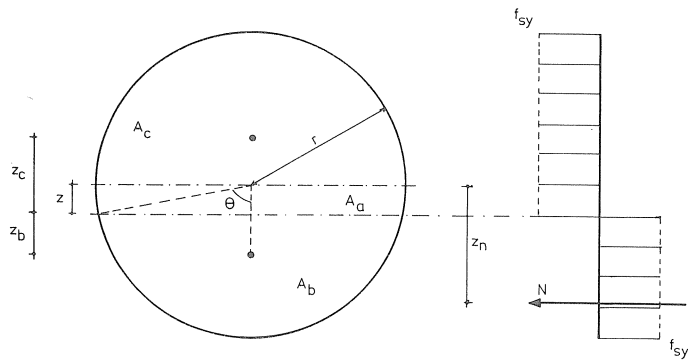

Fig. 4.18. Shift of the neutral axis.

To obtain equilibrium the bond force N must be equal to $2A_a \cdot f_{sy}$. Now, according to the equilibrium condition it follows:

$$\Sigma N = 0: (A_a + A_c)f_{sy} = (A_b + 2A_a)f_{sy} \tag{4.9a}$$

$$\Sigma M = 0: (A_a + A_c)f_{sy} \cdot z_c + A_b f_{sy} \cdot z_b + 2A_a f_{sy}(z_n - z) = M_u \tag{4.9b}$$

with

$$A_a = \frac{\pi}{2} r^2 - A_b \tag{4.9c}$$

$$A_b = r^2[\theta - 0.5 \sin(2\theta)] \tag{4.9d}$$

$$A_c = 0.5\pi r^2 \tag{4.9e}$$

$$z_b = \frac{0.67r^3 \sin^3(\theta)}{A_b} - z \tag{4.9f}$$

$$z_c = \frac{0.67r^3 \sin^3(\theta)}{A_a + A_c} + z \tag{4.9g}$$

For a bare bar, the following expression is valid:

$$(A_a + A_c)f_{sy}z_c = A_b f_{sy}z_b + 2A_a f_{sy}(z_n - z) \quad \text{with} \quad z = 0 \tag{4.9h}$$

Since in the case of a bar in concrete it is expected that the shift of neutral axis remains small, it is assumed that equation (4.9h) provides a satisfactorily close prediction for a dowel in concrete.

The plastic moment can now be calculated as a function of z_n which is related to the radius of the bar r, see Fig. 4.19. The shift of the neutral axis of the bar can be determined if the eccentricity of the bond force is known. The eccentricity of the bond force is related to the distribution of the bond stresses. This distribution is not exactly known, but can be determined with reasonable accuracy.

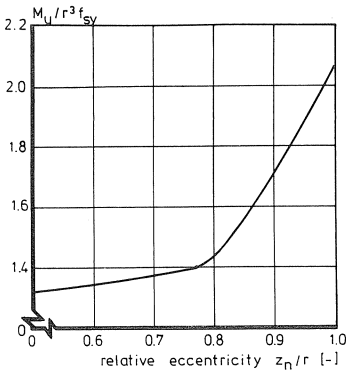

Fig. 4.19. The plastic moment as function of the eccentricity of the bond force z_n.

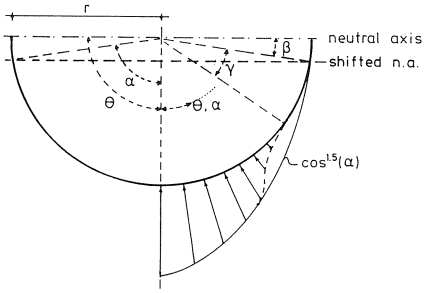

Fig. 4.20. The distribution of the bond stresses.

First, the bond stresses are related to the steel strain. Therefore, the bond stress is proportional to $r \cos(\alpha)$, see Fig. 4.20. Second, the bond stress is influenced by the normal pressure on the bar. Untrauer [44] found that the bond stress is proportional to $\sqrt{\sigma_n}$. According to a linear elastic response, the normal stress can be approximated by:

$$\sigma_n = \frac{\Delta D}{\pi r} \cos(\alpha) \tag{4.10}$$

Thus yielding for the bond stress:

$$\tau_{bond} = f(\cos^{1.5}(\alpha)) \tag{4.11}$$

The magnitude of the eccentricity of the bond force can now be calculated (see Fig. 4.20) according to:

$$z_n = r \frac{\int_0^{\pi/2-\beta} \tau_{bond} \cos(\theta)\, d\theta}{\int_0^{\pi/2-\beta} \tau_{bond}\, d\theta} = r \frac{\int_0^{\pi/2-\beta} \cos^{1.5}(\alpha) \cos(\theta)\, d\theta}{\int_0^{\pi/2-\beta} \cos^{1.5}(\alpha)\, d\theta} \tag{4.12a}$$

with

$$\alpha = \frac{\pi}{\pi - 2\beta} \theta$$

The steel close to the shifted neutral axis of the bar will slip relative to the concrete due to the reduced bond as a result of the low normal stresses. Therefore, the concrete in the vicinity of the shifted neutral axis will provide only a minor contribution to the bond force. This is shown by the broken line in Fig. 4.20, assuming that for an angle γ there is little bonding between steel and concrete. Now, equation (4.12a) becomes:

$$z_n/r = \frac{\int_0^{\pi/2-\beta-\gamma} \cos^{1.5}(\alpha) \cos(\theta)\, d\theta}{\int_0^{\pi/2-\beta-\gamma} \cos^{1.5}(\alpha)\, d\theta} \tag{4.12b}$$

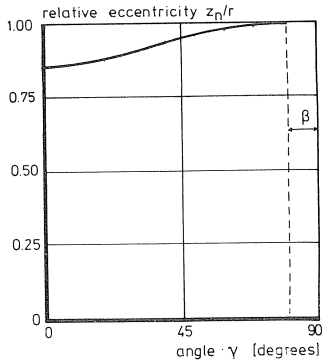

Fig. 4.21. The eccentricity of the bond as function of γ.

Equation (4.12b) is shown in Fig. 4.21 for β equal to 10 degrees. With the eccentricity of the bond force taken to be equal to the average value of $0.93r$, it is found in Fig. 4.19 that the plastic moment is equal to:

$$M_u = 1.78r^3 f_{sy} = 0.233\phi^3 f_{sy} \tag{4.13}$$

Note that the plastic moment is 34% higher than the plastic moment of the bare bar according to the theory of plasticity. In this case the neutral axis is shifted over a distance equal to $0.14r$. In consequence β is equal to 8° which is in good agreement with the assumption of 10°. Now, the equilibrium according to Fig. 4.16 becomes:

$$F_{du}(e + aX) = 0.223\phi^3 f_{sy} \tag{4.14}$$

and

$$F_{du} = X f^*_{ccyl} \phi \tag{4.15}$$

in which

f^*_{ccyl} = mean compressive strength of the multi-axially loaded concrete

Combining equations (4.14)–(4.15) yields:

$$F_{du} = 0.5C[\sqrt{4 \times 0.223 + (C\varepsilon)^2} - C\varepsilon]\,\phi^2 \sqrt{f_{sy} f_{ccyl}} \quad [\text{N}] \tag{4.16}$$

in which

$C = \sqrt{n/a}$ = empirical constant

$n = f^*_{ccyl}/f_{ccyl}$

$\varepsilon = \dfrac{e}{\Phi}\sqrt{\dfrac{f_{ccyl}}{f_{sy}}}$

ϕ, e in [mm], f_{ccyl}, f_{sy} in [MPa]

The constant C can be solved empirically by means of the experimental results of Rasmussen. Assuming zero-eccentricity, Rasmussen found from these test results:

$$0.5C\sqrt{4 \times 0.223} = 1.3 \tag{4.17}$$

Thus C is equal to 2.75. However, some eccentricity was inevitable during these tests. Therefore:

$$0.5C[\sqrt{4 \times 0.223 + (C\varepsilon)^2} - C\varepsilon] = 1.3 \tag{4.17a}$$

According to Rasmussen's formula the ultimate dowel is equal to:

$$F_{du} = 1.3\phi^2\sqrt{f_{sy}\, f_{ccyl}} \quad [\text{N}] \tag{4.18}$$

Assuming that the contact zone between the bar and the loading frame is loaded beyond its yielding strain up to the ultimate strain, the length of the contact zone can be determined. For the steel used in Rasmussen's tests the ratio between the yield strength and ultimate strength was approximately 0.6. Now, the eccentricity (see Fig. 4.22) becomes:

$$e = 0.5L = \frac{0.5F_{du}}{\phi f_{sy}/0.6} \quad [\text{mm}] \tag{4.19}$$

thus

$$e = 0.39\phi\sqrt{\frac{f_{ccyl}}{f_{sy}}} \quad [\text{mm}]$$

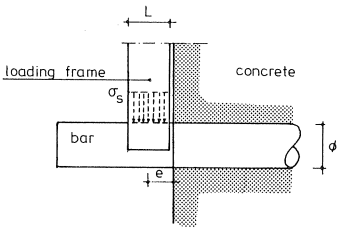

Fig. 4.22. Load eccentricity in Rasmussen's tests.

The average value of the ratio between steel strength and concrete strength was equal to 10.77 for the tests of Rasmussen. Now, combining equations (4.17a) and (4.19) yields:

$$C = 3.1$$

Thus:

$$F_{du} = 1.55[\sqrt{0.892 + (3.1\varepsilon)^2} - 3.1\varepsilon]\phi^2\sqrt{f_{sy}\, f_{ccyl}} \quad [\text{N}] \tag{4.20a}$$

with

$$\varepsilon = \frac{e}{\Phi}\sqrt{\frac{f_{ccyl}}{f_{sy}}}$$

$$F_{du} = 1.35[\sqrt{1+9\varepsilon^2} - 3\varepsilon]\phi^2\sqrt{f_{sy}\, f_{ccm}} \quad [\text{N}] \tag{4.20b}$$

with

$$\varepsilon = \frac{e}{\Phi}\sqrt{\frac{f_{ccm}}{f_{sy}}}$$

In Fig. 4.23 equation (4.20b) is compared with the available test results of Bennett [1], Paulay [32], Rasmussen [35], Vintzeleou [46] and Utescher [45]. It was found that for 76 experimental results the average ratio between the theoretical and the experimental dowel force was equal to 0.998 with a coefficient of variation of 17.2%. Lit [34] presents detailed information on these tests. Now the model will be extended to the case of a combined axial and lateral load. In practice, axial steel stresses develop because embedded reinforcing bars crossing the crack plane are strained due to the crack opening during shear sliding. In consequence, this increasing axial steel-tensile force will influence the equilibrium of forces and bending moments in the bar. The axial steel force will achieve equilibrium with axial stresses in the vicinity of the (shifted) neutral axis of the bar, see Fig. 4.24. Fig. 4.24 is similar to Fig. 4.18 except for the influence of the axial force. The contribution of the axial force to the equilibrium can be easily taken into account in equations (4.9a–h). Fig. 4.25 presents the influence of the axial force upon the magnitude of the ultimate dowel force. For small values of the axial force the shift of the neutral axis is hardly influenced. For increasing axial force the shift of the neutral axis decreases, until it reaches zero for an axial force equal to the yield force, see Fig. 4.26.

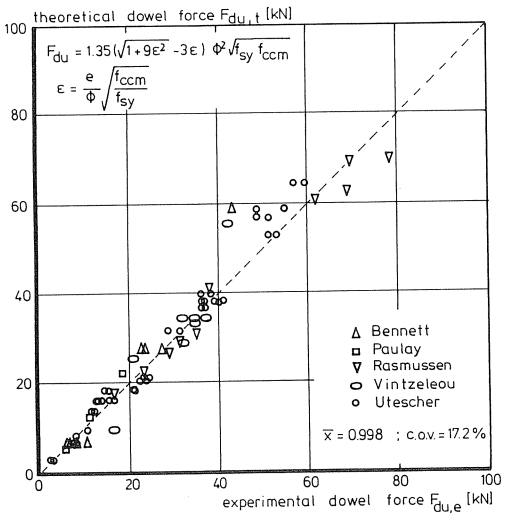

Fig. 4.23. Comparison of the experimental and theoretical results.

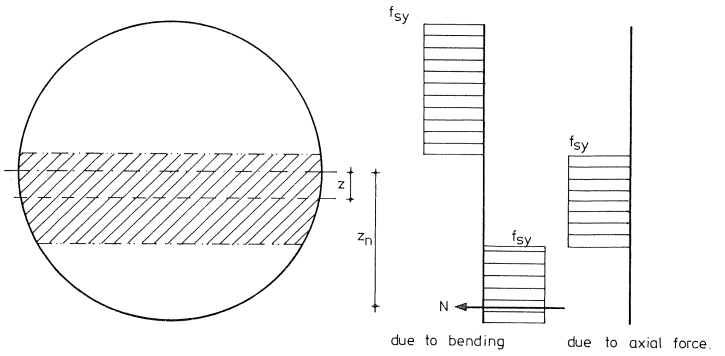

Fig. 4.24. Equilibrium of the forces in the plastic hinge.

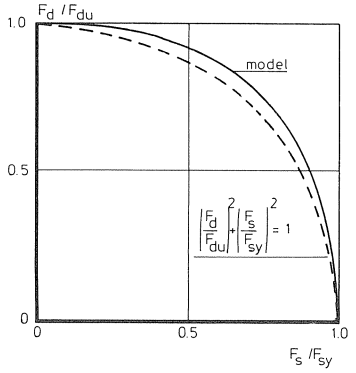

Fig. 4.25. The dowel force as a function of the axial steel force.

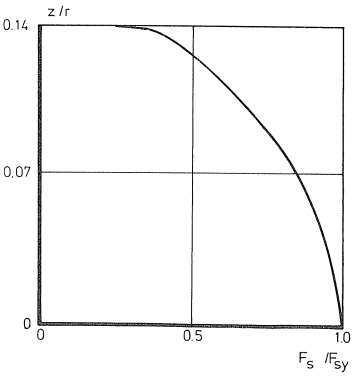

Fig. 4.26. The shift of the neutral axis as a function of the axial force.

The interaction between the axial steel force and the ultimate dowel force can be satisfactorily predicted by equation (4.21) proposed by Vintzeleou [46] in which n and m are equal to 2. See Fig. 4.25:

$$\left(\frac{F_d}{F_{du}}\right)^n + \left(\frac{F_s}{F_{sy}}\right)^m = 1 \quad \text{or} \quad \gamma_d = \sqrt[n]{1 - \left(\frac{F_s}{F_{sy}}\right)^m} \tag{4.21}$$

in which

F_d = dowel force
F_{du} = ultimate dowel force according to equation (4.20b)
F_s = axial steel force
F_{sy} = steel yield force
$\gamma_d = F_d/F_{du}$

Equations (4.20b) and (4.21) can be combined for the ultimate dowel force, thus yielding an expression for bars with an axial steel force. This expression is compared with

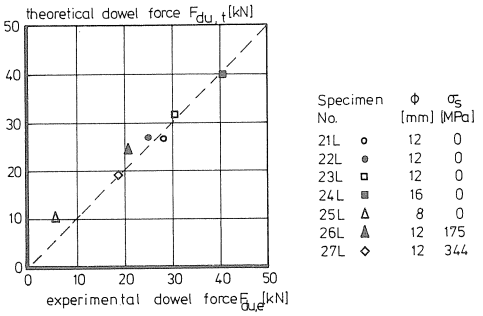

Fig. 4.27. The experimental and theoretical results for Millard's tests [26].

experimental results of Millard [26], see Fig. 4.27. The experimental result of test 25L is obviously abnormal. This was probably due to the fact that for the small 8 mm diameter bar used in this test, the strain gauges were stuck to the surface of the bar, thus influencing the bonding of the bar to the concrete.

If this result is disregarded, an average ratio of the predicted to the experimentally obtained dowel strength is found which is equal to 1.02 with a coefficient of variation of 8.1%.

Detailed information is presented in [34].

In the case of cyclic dowel loading, numerous tests [9, 16, 46] have not yet yielded a fundamental insight into the physical behaviour of dowels embedded in concrete and subjected to cyclic loads. Therefore, empirical expressions for the dowel stiffness are derived for practical use. Vintzeleou [48] proposed a formalistic model for fully reversed shear displacements, see Fig. 4.28.

Vintzeleou's formalistic model can be easily implemented into numerical programs. However, there is still a need for a more theoretical approach to the behaviour of a dowel subjected to cyclic loads. Therefore, an attempt is made to derive a model largely based upon material behaviour. Fig. 4.29 shows the mechanism of loading and unload-

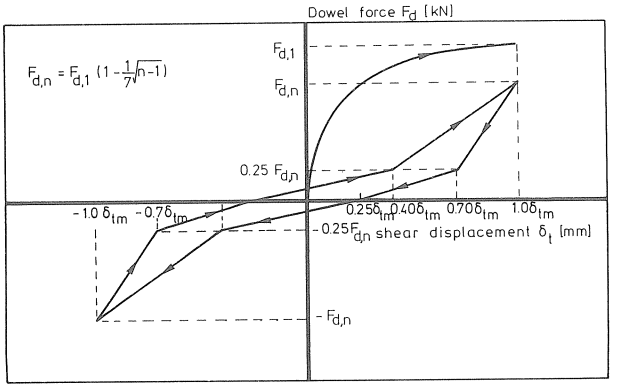

Fig. 4.28. Formalistic model for fully reversed shear displacements as proposed by Vintzeleou [48].

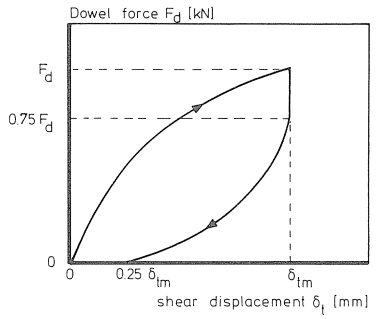

Fig. 4.29. Mechanism of loading and unloading in the first cycle.

ing in the first cycle. For the maximum applied dowel force, high triaxial stresses support the bar. After reaching the maximum dowel force, the force decreases. Now, the triaxial stress state first rapidly loses its confinement.
In consequence, the dowel force can decrease without (hardly) any restitution of the concrete deformation, see Fig. 4.29.
The drop in concrete stress is strongly related to the loading path of the concrete. For triaxially loaded concrete, Van Mier [25] found that at the moment of unloading a sudden stress drop occurs. This causes a drop in dowel force, which was found to be approximately 25% of the maximum dowel force. After that, the shear displacement decreases with decreasing dowel force. Some non-recoverable shear displacement remains for zero-dowel force, which is about 25% of the maximum shear displacement. For a fully reversed dowel force, the deformed matrix material after unloading is shown in Fig. 4.30.
Upon re-loading in the positive direction, the bar initially responds as a beam partially fixed at one side, see Fig. 4.31. For this loading situation, the dowel stiffness is determined by linear elastic material behaviour and can be expressed by:

$$K_1 = \frac{3\phi^4 E_s}{60\phi L^2 + 40L^3} \quad [\text{N/mm}] \tag{4.22}$$

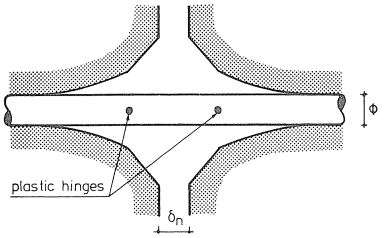

Fig. 4.30. Matrix deformation after a load cycle.

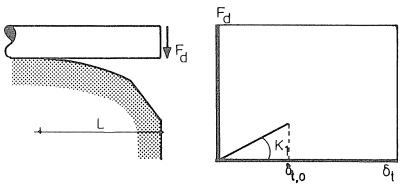

Fig. 4.31. Initial dowel stiffness K_1.

On the basis of the experimental results of Vintzeleou [46] an experimental relation was derived for L:

$$L = 2.56\phi\sqrt{\delta_{t,max}}(n-1)^{0.1} \quad [\text{mm}] \tag{4.23}$$

with

$\delta_{t,max}$ = maximum shear displacement in previous cycle
n = number of cycle; Note that the first load cycle in the negative direction is cycle 2. In consequence, the second cycle in the positive direction is cycle 3. In the case, where the imposed displacement in the negative direction is, for instance 50% of the displacement in the positive direction, the cycle in the negative direction is cycle 1.5. The second cycle in the positive direction is then cycle 2.5 and so on

The term $(n-1)^{0.1}$ in equation (4.23) accounts for the fatigue of the concrete underneath the bar. Because of the fact that for increasing dowel displacements, previously strained matrix material is crushed and unaffected material is loaded, the number of cycles can be reset to 1 in the case of load-controlled tests.

The stiffness K_1 determines the dowel response until the shear displacement $\delta_{t,0}$ is reached, see Fig. 4.31. For this shear displacement, the bar is supported by the concrete over the length $L - \phi$, see Fig. 4.32.

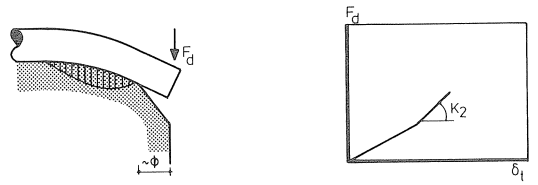

Fig. 4.32. The dowel stiffness K_2.

Due to the support of the concrete, the dowel stiffness increases until it becomes equal to stiffness K_2. The response of the concrete is approximated by regarding the bar as a beam on an elastic foundation. As stated above, the coefficient of the subgrade reaction is related to the dowel displacement. The following expression is derived:

$$K_f = 390(\delta_t^*)^{-0.78} \quad [\text{MPa/mm}] \tag{4.24}$$

However, in this expression the shear displacement does not include the slip related to K_1. Substitution of δ_t^* by an average value of $0.3\delta_{t,max}$ yields:

$$K_f = 998(\delta_{t,max})^{-0.78} \quad [\text{MPa/mm}] \tag{4.24a}$$

Because the subgrade reaction is proportional to the modulus of elasticity, which is approximately proportional to the square root of the concrete grade, the following expression is obtained:

$$K_f = 168\sqrt{f_{ccm}}(\delta_{t,max})^{-0.78} \quad [\text{MPa/mm}] \tag{4.24b}$$

Accounting for the load eccentricity, the dowel stiffness can be expressed by

$$K_2 = 55\phi^{1.75} f_{ccm}^{0.375} \delta_{t,max}^{-0.59} \quad [\text{N/mm}] \tag{4.24c}$$

This stiffness is valid until the plastic hinge develops. As in this state there is still no contribution of the concrete to the section modulus of the bare bar, the dowel force at the onset of yielding is:

$$F_{d,sy} = M_{sy}/e = 0.1\phi^2 f_{sy} \quad [\text{N}] \tag{4.25}$$

Because of the development of the plastic hinge, the bar makes contact with the concrete close to the crack plane, see Fig. 4.33. For the coefficient of subgrade for this part of the concrete equation (4.24b) can again be used. This part of the concrete now determines the dowel stiffness. As it has been observed that the 25% of the maximum shear displacement is non-recoverable, it is assumed that the deformation of the concrete over the length $L - \phi$ contributes 25% of the total shear displacement. Thus, the dowel stiffness K_3 is expressed by:

$$K_3 = 0.75 \cdot 168\phi^{1.75} f_{ccm}^{0.375} \delta_{t,max}^{-0.59} = 126\phi^{1.75} f_{ccm}^{0.375} \delta_{t,max}^{-0.59} \quad [\text{N/mm}]$$

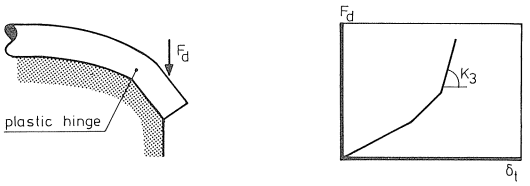

Fig. 4.33. The dowel stiffness K_3.

The total loading path according to the proposed model is shown in Fig. 4.34. Unloading causes a drop in dowel force of 25% of the maximum value. Subsequently, the unloading stiffness is equal to K_3 until $F_{d,sy}$ is reached. Finally, the stiffness K_2 is used to obtain zero-dowel force. In the case of a repeated dowel force, the response is calculated according to the model for reversed dowel loads. However, the stiffness K_3 is used to connect the zero-stress state to the re-loading branch, see Fig. 4.34a. Apart from that, another restriction should be made. The dowel force is not allowed to exceed 85% of the dowel force for the monotonic case, see Fig. 4.34b. The stiffness is then equal to the stiffness K_4, which was found for the monotonic case for the given shear displacement. Fig. 4.35 presents a comparison of this model with experimental results of Vintzeleou [46] and Jimenez [16]. This corresponds fairly well with the experimental results. Jimenez's test results shows that the model can also be applied to the case of imposed dowel loads. From the monotonic dowel tests of Eleiott [9] it is known that the dowel stiffness is strongly influenced by the magnitude of the axial steel force, and so the following expression is proposed to reduce the dowel stiffness:

$$\gamma_k = \left(1 - \frac{F_s}{F_{sy}}\right)^{0.5} \tag{4.27}$$

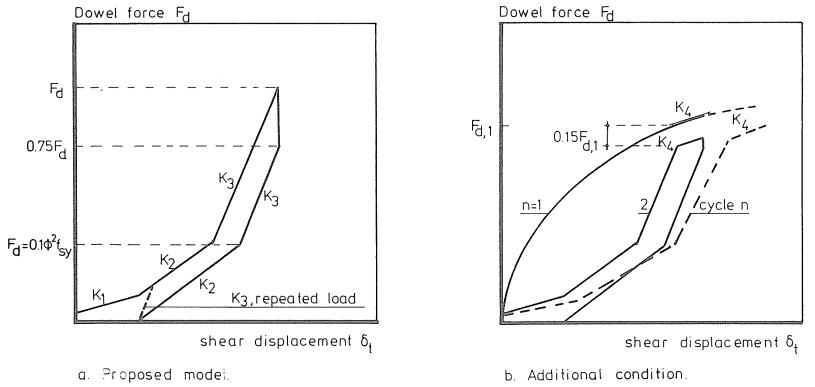

Fig. 4.34. Loading and unloading according to the model.

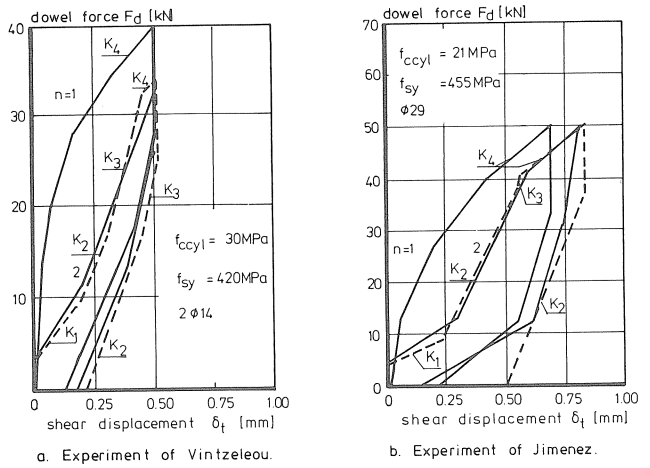

Fig. 4.35. Comparison of experimental results with the proposed model.

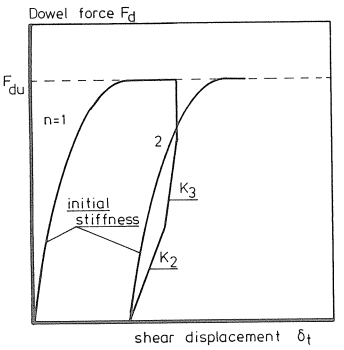

Fig. 4.36. The model in the case where the dowel strength is reached.

A special situation arises when the dowel strength F_{du} is obtained in a cycle. In this case the whole cross-sectional area of the bar will yield. In the case of a reversed dowel force, the only restriction is that the force cannot exceed the dowel strength. However, in the case of a repeated dowel force, the yield of the bar strongly influences the bar stiffness. In this case the bar remains in close contact with the supporting concrete, thus approximating the situation in the first load cycle. Because of the already deformed bar, this can be regarded as a shift of the initial stiffness of the bar, see Fig. 4.36. Now, the force-displacement relation for the static case must be applied.

4.4 *The combined mechanism of aggregate interlock and dowel action*

Vintzeleou [46] and Millard [27] have already demonstrated that the combined mechanism of aggregate interlock and dowel action is suitable for predicting the shear resistance of cracked concrete according to the equilibrium condition shown in Fig. 4.37. However, for push-off experiments with a very small initial crack width as performed by Walraven [54], their models underestimate the measured shear strength of the crack.

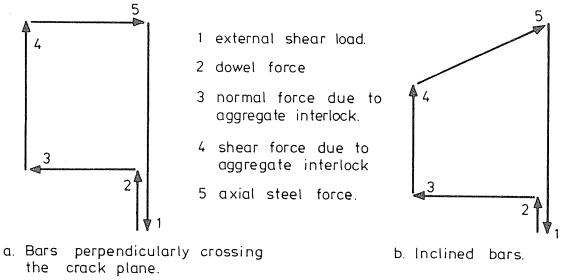

Fig. 4.37. The equilibrium condition for cracked reinforced concrete.

Furthermore, for practical use the equilibrium presented in Fig. 4.37 can only be determined if the relation between the axial bar force and the crack width is known. The magnitude of the axial bar force can be calculated by means of the equilibrium with the normal force due to aggregate interlock. The bond characteristics for a bar subjected to the combined action of axial and dowel forces have not yet been determined experimentally. Due to the lack of knowledge about the actual bond behaviour, empirical relations are still used for describing the crack opening path. In this Section the previously described mechanisms will be combined, whilst also taking into account the magnitude of the initial crack width. In order to predict the crack response accurately, the effect of these mechanisms and of their interactions upon the crack opening direction must be known.

On the basis of the experimental results of tests on pre-cracked reinforced push-off specimens by Walraven [54] and Millard [27], it was concluded that the crack opening path followed during these tests ensured a constant contribution by the aggregate interlock mechanism to the transferred shear stress. The plastic hinges in the bars due to the

dowel action are already developed during this phase. According to Walraven's two-phase model, this crack opening path followed in a displacement-controlled test requires the minimum amount of energy.
For Walraven's experiments, Fig. 4.38 presents the calculated and experimental crack opening paths.
Furthermore, the calculated crack opening direction explains the difference in crack opening paths obtained in the experiments of Walraven [54] and Millard [27].
The maximum particle diameter used by Walraven and by Millard was 16 mm and 10 mm respectively. If allowance is made for the particle diameter, the crack opening paths can be calculated, see Fig. 4.39. These correspond well to the experimental results.

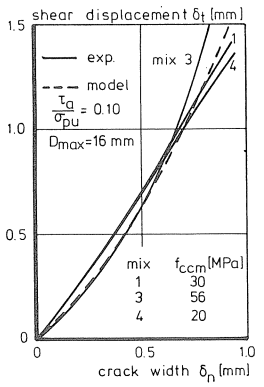

Fig. 4.38. Theoretical and experimental crack opening path for reinforced specimens [54].

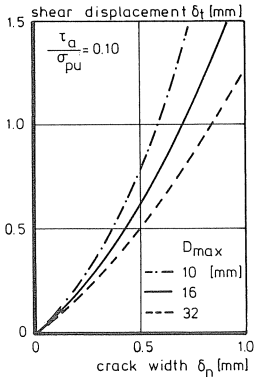

Fig. 4.39. The crack opening paths for different maximum particle diameters according to the two-phase model.

However, it appeared from the test results that the aggregate interlock mechanism provides a prediction of the crack opening direction for constant shear stress contribution only. For the phase in which there is an increasing contribution of the aggregate interlock to the shear transfer, the plastic hinge in the reinforcing bars is still developing. Therefore, the bars will also influence the crack opening direction. To account for this influence, the deformation of the bar due to the dowel force is roughly approximated by:

$$\delta_t = \sqrt{\frac{\delta_{no} f_{sy}}{2 f_{ccm}}} (\delta_n - \delta_{no})^{0.667} \qquad [\text{mm}] \tag{4.28}$$

with

δ_{no} = initial crack width

Applying equation (4.28) provides combinations of the crack displacements. The contribution of the aggregate interlock mechanism to the shear transfer can now be calculated according to the two-phase model.
At the onset of a decrease in shear stress, the crack opening direction is fully determined by the aggregate interlock mechanism, as is shown in Fig. 4.40a.

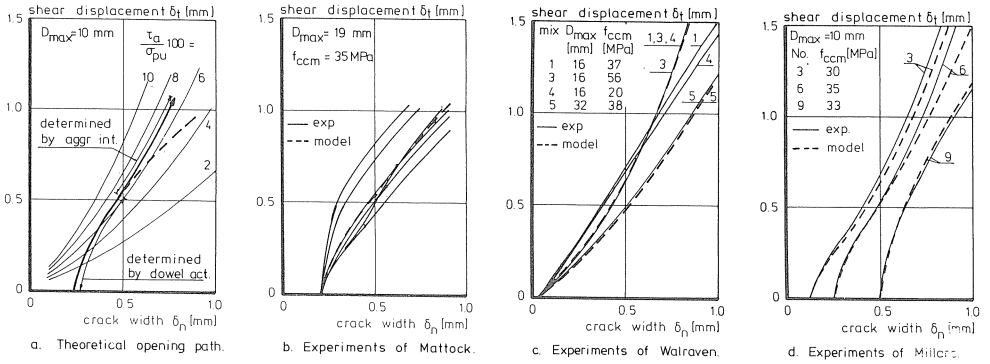

Fig. 4.40. Theoretical and experimental crack opening paths.

During this phase, the equilibrium condition in the bar is determined by the axial steel force. The bar itself does not influence the crack opening path, due to the plastic hinge, which is now fully developed. In the plastic hinge any combination of the axial bar force and the dowel force according to equation (4.21) is possible.

Fig. 4.40b–d presents a comparison of the calculated crack opening paths with opening paths experimentally obtained by Millard [27], Mattock [23] and Walraven [54].

There is reasonable agreement between the calculated and experimental crack opening paths. During the phase of increasing shear stress the contribution of the dowel action mechanism to the shear transfer also increases.

An empirical relation is given by:

$$\frac{D_d}{F_{du}} = \sqrt[3]{\frac{\delta_t}{\delta_{no} + \delta_{t,e}}} < 1 \tag{4.29}$$

with

$$\begin{aligned} \delta_{t,e} &= \text{maximum slip occurring during the elastic deformation} \\ &= 1.31 \cdot 10^{-7} \phi^{0.60} (f_{ccm} f_{sy})^{1.2} \text{ [mm]} \end{aligned} \tag{4.30}$$

For a large crack width, equation (4.30) decreases in importance in proportion to the crack width.

Here, the crack opening path can be described according to the transfer mechanisms. However, the bars crossing the crack plane restrain the crack opening due to normal stress caused by the mechanism of aggregate interlock. For increasing crack displacement this normal stress can become so high that the restraining force in the bars is equal to the yield force. A further increase in crack displacements should fulfill the equilibrium condition according to Fig. 4.37. Therefore, it was expected that the crack opening direction would now be determined by a constant contribution of the aggregate interlock mechanism to the normal stress. However, it was found experimentally [54] that the crack opening path was hardly affected by the yielding of the bars. This can be easily explained by Walraven's two-phase model.

Where yielding of the bars occurs, the increase in crack width exceeds the increase in

shear slip, thus causing a dramatic decrease in the magnitude of the contact areas. In consequence, the normal stress decreases and reaches equilibrium with the yield strength in the bars. Due to the decrease in contact areas the shear stress also decreases. According to the two-phase model this decrease is less pronounced than the decrease of normal stress.
However, to provide an easy calculation method, the reduction in shear stress is related to the decrease in normal stress.
This yields:

$$\gamma_a = \frac{f_{sy}}{\sigma_s} = \frac{\varrho f_{sy}}{\sigma_a} \tag{4.31}$$

Now, the combined mechanism will be shown by means of an example of Walraven's test specimen No. 110208t. For this test, the cube compressive strength was 35.9 MPa. The maximum particle diameter was 16 mm.
The steel yield strength was equal to 360 MPa.
Four 8 mm bars were used, corresponding to a reinforcement ratio of 0.0056. The externally measured shear stress consists of the contributions of dowel action and aggregate interlock according to:

$$\tau_{cal} = \gamma_a \tau_a + \gamma_d \tau_d \tag{4.32a}$$

$$\sigma_{cal} = \gamma_a \sigma_a \tag{4.32b}$$

with

τ_a = according to equation (4.1a), σ_a according to equation (4.1b)
γ_a = according to equation (4.31)
τ_d = according to equation (4.20b) (F_d/shear area)
γ_d = according to equation (4.21)

The theoretical crack opening path is calculated according to equation (4.29) and according to Fig. 4.4 where τ_a is equal to 3.8 MPa. The theoretical results are in reasonable agreement with the experimental results. This holds true for both the crack opening path and the shear stress-crack width relation. Both relations are shown in Fig. 4.41a-b. Fig. 4.41 presents the comparison between a few experimental and calculated results. The calculations for these tests are carried out in the same way as has been done for specimen No. 110208t. The agreement between the calculated and experimental results is quite satisfactory.
In the case of the cyclic loads, the crack opening path or the normal stress-crack width relation must be input in the calculation. Unfortunately, contrary to the static crack opening path, the crack opening direction in a cyclic shear loading experiment cannot be determined without exactly knowing the normal stress-crack width relation. The normal stress was, however, not recorded during the tests reported in the literature. In order to obtain information on this normal restraint stiffness for reinforced concrete, some additional tests were performed with bars prepared with a bolt gauge situated in the crack plane, see Chapter 3.

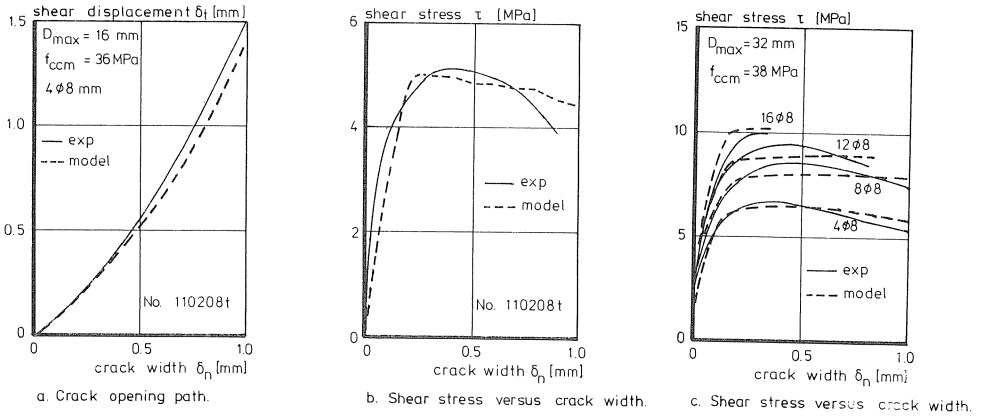

Fig. 4.41. Comparison of the experimental and calculated results.

It was found that that the normal stress can be approximately related to the crack width; see Fig. 4.42:

$$\sigma_n = \alpha \varrho f_{sy}(\delta_n - \delta_{n,o}) \qquad \text{(MPa)} \tag{4.33}$$

with

$\alpha = 0.25$ (mm^{-1}) for "low-intensity high cycle fatigue"

$\alpha = \dfrac{3}{n+2} > 0.25$ for "high-intensity low cycle" fatigue

n = number of cycles (fully reversed)

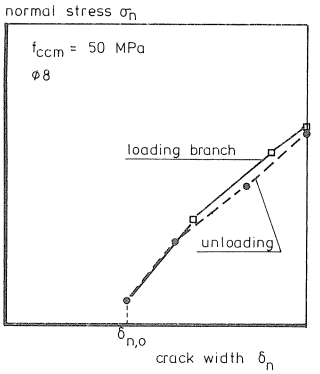

Fig. 4.42. The relation between normal stress and crack width during cycling [11].

The normal stiffness according to equation (4.33) was applied to the tests of Jimenez et al. [20].
The cylinder compressive strength of the concrete used was approximately 23 MPa, the steel yield strength was 455 MPa. In test No. 5 the initial axial steel stress was 331 MPa.

The specimen was reinforced by means of four 22 mm diameter bars ($\varrho = 1.08\%$). The experimentally obtained and the calculated response for cycle number 15 is shown in Fig. 4.43. The calculated response is in reasonable agreement with the experimental result, although the calculated response is a little bit too soft. The end-displacements in each cycle are satisfactorily predicted. The load was fully reversed, but only the response in the positive direction is shown. The crack response in the opposite direction might be slightly different due to the position of the bars with respect to the casting direction.

Because of this, the bars may have a different support of the concrete in both directions. The calculation yielded information about the contributions of both transfer mechanisms to the externally applied load. The contributions of both mechanisms were found to remain nearly constant during cycling.

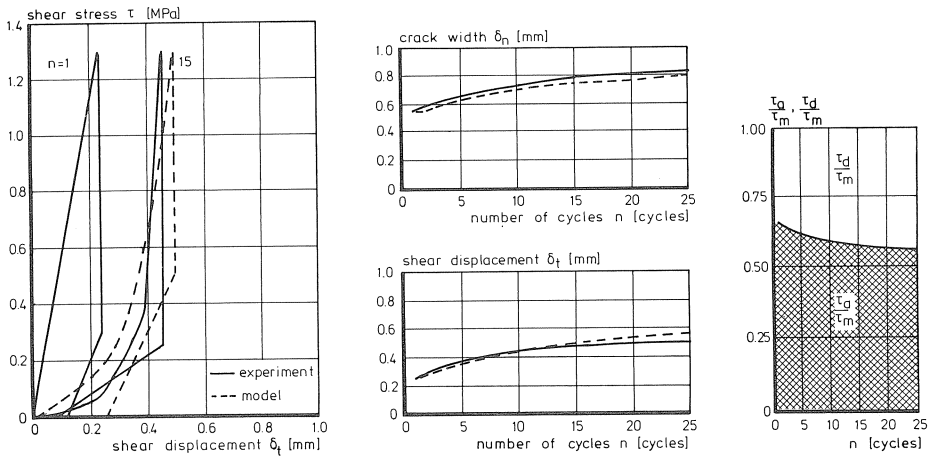

Fig. 4.43. Test No. 5 of Jimenez [20] compared with the proposed model.

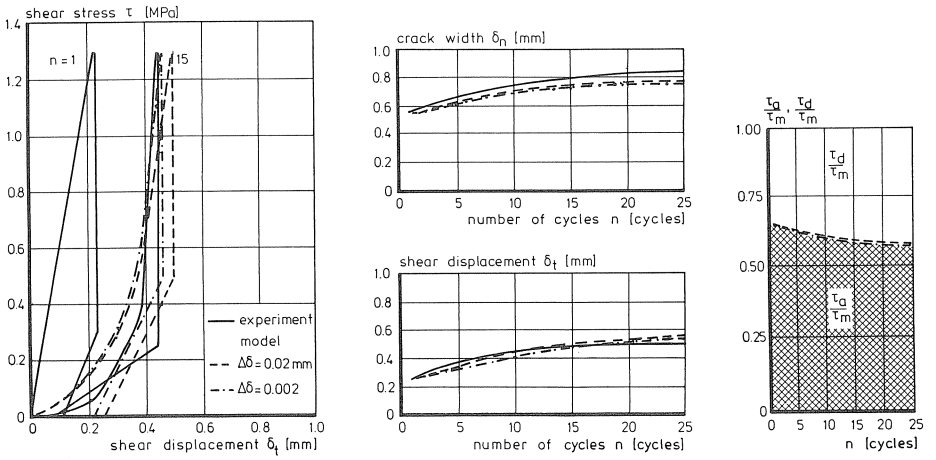

Fig. 4.44. Test No. 5 with different displacement increments.

For this experiment the aggregate interlock mechanism transfers approximately two-thirds of the total shear load. The sensitivity of the model was investigated by performing the same calculation with two different displacement increments. The results are shown in Fig. 4.44. The differences between both calculations are in fact negligible. The combined model proposed in this Section can of course be applied to the case of "low-intensity high-cycle" fatigue. Experiments of this type are described in Chapter 3. The experimentally obtained crack displacements must, however, be larger than the smallest displacements which can accurately be predicted by the model. Therefore, some cycles approaching shear failure are simulated so as to ensure a sufficient increase in the crack displacements in each cycle. Again, the normal restraint stiffness according to equation (4.33) was used in the calculation.

The cycles 640 and 1620 of test No. A/6H/.66/7.9/.03 are considered (page 57, [33]), see Fig. 4.45. The maximum repeated shear stress applied during cycling was 7.9 MPa. The cube compressive strength was 48.0 MPa. The crack plane was reinforced by means of twelve 8 mm diameter bars with a yield strength of 550 MPa. For the cycles considered, the shear displacement largely exceeds the shear displacement for which the ultimate dowel strength is obtained for a monotonic increasing shear load.

Therefore, it is expected that a large plastic deformation has occurred in the plastic hinges in the reinforcing bars. For the calculation process this plastic deformation is accounted for by applying the static dowel action model to the measured shear displacement at zero stress according to Fig. 4.36. Furthermore, the measured crack width at zero stress was input into the calculation. The theoretical results are also presented in Fig. 4.45, showing a reasonable agreement with the results obtained experimentally. Because of the large contribution of the dowels to the transfer of shear stress, restitution of the shear slip during unloading starts at 75% of the shear load, as is predicted by the dowel action model.

For tests of this type, in which the contribution of the dowel mechanism to the shear transfer is equal to its ultimate value, an interesting scenario for the tests can be found.

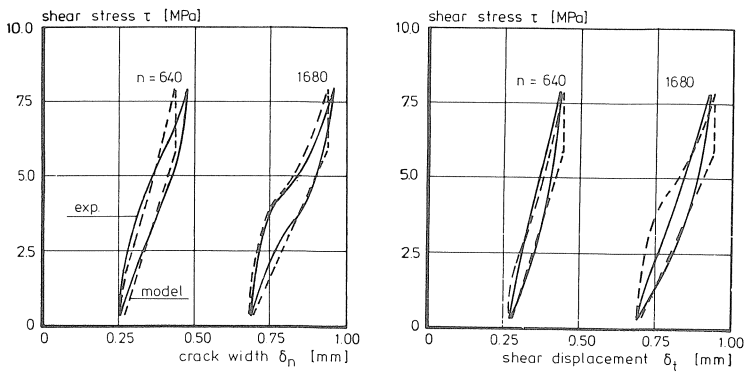

Fig. 4.45. Test No. A/6H/.66/7.9/.03 compared with the proposed model [33].

During the first few cycles the mechanism of aggregate interlock transfers the difference between the applied shear stress and the ultimate dowel stress.
The combination of the end-displacements in these cycles will be determined by the matrix strength and the maximum particle size according to Fig. 4.4. In view of the fact that the contribution of aggregate interlock to the shear stress transfer remains constant during cycling, it can be expected that the crack opening path is determined by a constant ratio of τ_a to σ_{pu}.
On the basis of this assumption it can be easily checked whether the tests described in Chapter 3 are in agreement with the proposed model. For all the tests, the crack opening path should follow the theoretical opening path for a constant ratio $(\tau_m - \tau_{pu})/\sigma_{pu}$. In Fig. 4.46 a few typical test results are compared with this assumption. It was found that for a total of 42 repeated loading tests, 16 experimental crack opening paths are in close agreement with the theoretical opening path. There is reasonable agreement for three tests, while the difference between the result of six tests and the model can easily be explained. In 12 experiments the measured displacements were too small to draw any conclusions.

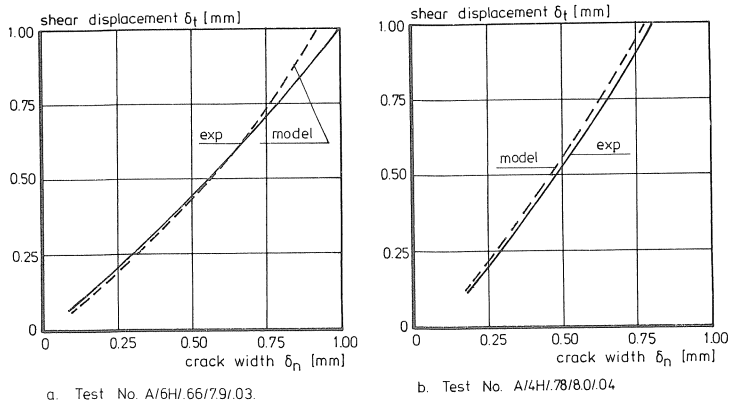

Fig. 4.46. The experimental crack opening path compared with the opening path according to the model.

In consequence, only five measured crack opening paths showed large deviations from the theoretical crack opening paths. From these results it can be concluded that also in the case of "high-cycle" repeated shear loading the crack opening direction is determined by a constant ratio between τ_a and the matrix strength σ_{pu}.

4.5 *Concluding remarks*

Shear stress transfer in cracked reinforced concrete depends upon the aggregate interlock mechanism and dowel action. The interaction between both mechanisms is determined by the equilibrium of forces normal to the crack plane. The static crack opening path is initially determined by the bar deformation until the plastic hinges in the bar

have been fully developed. Subsequently, the crack opening direction is related to a constant contribution of the aggregate interlock mechanism to the shear transfer. In the case of cyclic loads it was found that the model as developed, predicts a constant ratio between the shear stress transferred by aggregate interlock and the dowel stress. Furthermore, it was found that in the case of plain concrete the load history can be accounted for by the end-displacements of the crack in the previous load cycle. The simple quasi-static calculation according to the reduced contact model for the aggregate interlock mechanism provides good predictions of the crack response during cycling. However, a simplified model cannot be used as general as the original two-phase model.

5 Further interpretations

5.1 *Introduction*

This chapter deals with some aspects of the models developed. First, the case of inclined bars subjected to static shear loading is discussed.
Second the measured steel stress in the reinforced specimens is analyzed using the model for aggregate interlock and dowel action.
Finally, the cyclic tests on plain concrete are evaluated.

5.2 *Inclined reinforcing bars*

Fig. 5.1 represents a bar with an angle of inclination to the crack plane. The bar is subjected to a load F_{ext} parallel to the crack plane. According to Vintzeleou [46], the concrete reaction force is provided by a layer of concrete with a depth equal to twice the bar diameter. For small bar inclinations the concrete supporting the bar in the vicinity of the crack plane has a depth which is much less than twice the bar diameter. Apart from that, inclined cracking can occur in the concrete.
In consequence, the ultimate dowel force will be less than the dowel resistance in the case of a bar perpendicular to the crack plane. The actual stress distribution in the concrete is not accurately known, so that the influence of the angle of inclination upon the concrete's response to a lateral bar displacement must be roughly estimated.
To account for this influence, the dowel resistance is related to the inclination according to:

$$F_{du} = F_{du,90} \sin(\theta) \tag{5.1}$$

In consequence the externally measured force is equal to $F_{du,90}$. Furthermore, the dowel force in the crack has an eccentricity e to the concrete. This eccentricity is equal to:

$$e = 0.5\phi \operatorname{cotan}(\theta) + 0.5\delta_n/\sin(\theta) = \text{approx. } 0.5\phi \operatorname{cotan}(\theta) \tag{5.2}$$

This eccentricity can now be inserted in equation (4.20b).

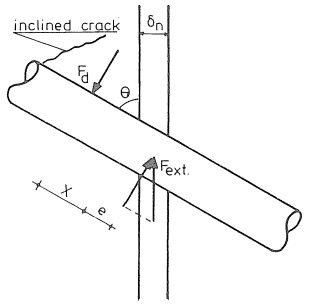

Fig. 5.1. Bar with a small angle of inclination.

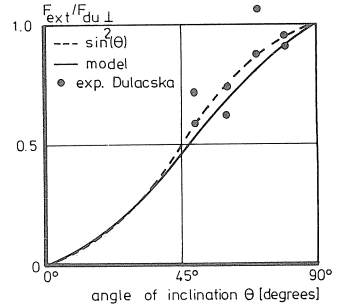

Fig. 5.2. Dowel strength related to angle of inclination.

The result is shown in Fig. 5.2 for the ratio f_{sy}/f_{ccm} which is equal to 10. The dowel force is taken as being proportional to the dowel force for a bar perpendicular to the crack plane with zero-eccentricity. It is shown that for the range of investigated by Dulacska [8], equation (5.2) provides a reasonable prediction of the experimental results.
Equation (5.2) is in close agreement with the reduction according to $\sin^2(\theta)$ as proposed by Mattock [22]. It can be concluded that the influence of small inclinations can be taken into account in equation (4.20b) with an additional eccentricity and by multiplying the resulting dowel force by $\sin(\theta)$. In the case of a large angle of inclination the additional eccentricity has a negative sign.

It can be expected that the response of the concrete lateral bar displacements is stiffer than for the bars perpendicularly crossing the crack plane. However, since this increase is limited to the concrete close to the crack plane, the increase in stiffness is less pronounced than the decrease in stiffness for small angles of inclination. The minor increase of concrete stiffness will be disregarded here. Again, the dowel force can be determined with equation (4.20b).

5.3 *Measured axial steel stress*

In Chapter 3 some additional detailed push-off tests are described, in which the steel strain was recorded using bolt gauges.
In theory, the bolt gauges, which were in the neutral axis of the bare bar, reflected the strain due to the equilibrium with the normal stress caused by aggregate interlock, However, according to the model of dowel action, the neutral axis was shifted to the supported side of the bar. As a result, the ends of the strain gauges were situated in regions in the bar which were highly strained. According to the model, the plastic hinges are situated rather close to the crack plane, so that the ends of the gauge nearly reached the yield strain. Thus, the average recorded strain according to the model will be considerably larger than is necessary to achieve equilibrium with the normal force due to aggregate interlock. Indeed, this phenomena was observed in the experiments. Taking into account the yield strength at the ends of the gauge, the average normal

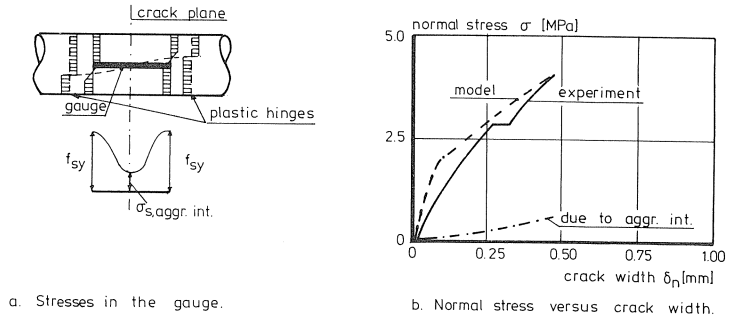

Fig. 5.3. Normal stress versus crack width for test D1 [11].

stress according to the model agrees reasonably with the experimental results, see Fig. 5.3.

5.4 *Analysis of the plain concrete tests*

For the test series on cracked plain concrete described in Section 3.3, no straightforward relationship was obtained between the stress level, the number of cycles and the crack displacements. Generally, the crack response was initially stiffer than could be expected on the basis of the two-phase model. This phenomenon is probably due to the relatively high initial normal stress, which was used in this test series. During cracking of the concrete prior to the actual push-off test, some matrix material and small particles will be completely torn out of the crack faces, as is shown theoretically by Termonia and Meakin [41]. Due to this material the crack cannot be re-closed to its original value. This rubble transfers the initial normal stress and is thereby pushed into the crack faces. A subsequent shear sliding will force this rubble to act like stiff struts transferring both normal and shear stresses. Five different stages can be distinguished. Initially, the struts only transfer normal stress, see Fig. 5.4a. A shear displacement will cause a rotation of these struts. In consequence, the struts provide a positive contribu-

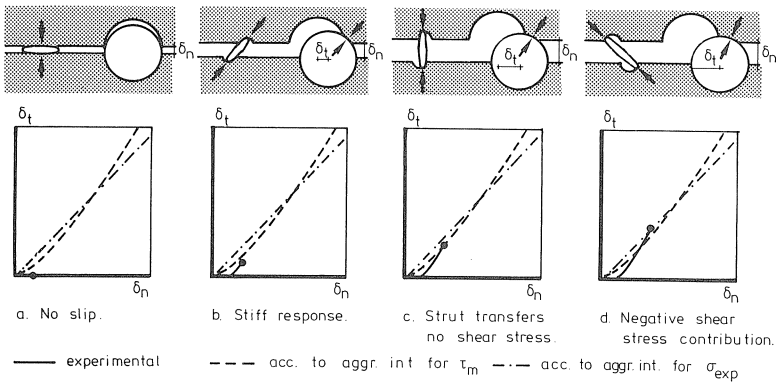

Fig. 5.4. The strut mechanism due to the initial normal stress.

tion to the transfer of shear stresses and determine the crack opening direction, see Fig. 5.4b. Simultaneously, the transfer of stresses due to aggregate interlock increases. For a given shear displacement the average orientation of the struts is perpendicular to the crack plane, see Fig. 5.4c. In this case only normal stress is transferred by the struts. A further increase in the shear displacement will cause a rapidly decreasing negative contribution of the struts to the shear transfer. A steep crack opening path is then obtained, see Fig. 5.4d.
Finally, the normal stress due to aggregate interlock is in equilibrium with the externally applied normal stress. The struts now become inactive, like in the case of a very low initial normal stress.
However, the crack opening direction is already determined by the struts. According to the two-phase model, a less steep crack opening direction will cause a sharp decrease in the shear stress transferred by the crack plane. Therefore, the steep crack opening path is followed despite the inactivity of the struts.

6 Conclusions

The transfer of the static and cyclic in-plane shear stresses in cracked reinforced concrete panels depends upon the combined mechanism of aggregate interlock and dowel action. The interaction between both these transfer mechanisms is caused by the equilibrium condition normal to the crack plane.
Experimental results as well as theoretical considerations lead to the conclusion that bond characteristics of embedded bars determined in an axial pull-out test cannot be applied to the case of shear sliding. The lack of experimental and theoretical knowledge about the proper bond characteristics is a major problem in describing the dowel action mechanism.
An important conclusion is that in this case of plain cracked concrete the load history is fully incorporated in the end crack displacements of the previous cycle.
For the stress levels investigated, no decrease in matrix strength was found. Further study is, however, necessary in this field. First, only one stress ratio was investigated. Second, a constant loading frequency was used in the test series.
Both parameters are expected to have a major influence on the stiffness degradation of the crack due to cycling. The cyclic aggregate interlock model is a highly simplified representation of the physical reality. This model is, however, applicable to a wide range of tests. The dowel action model for cyclic loads is partially based upon empirical relations, thus limiting its application.
Under special circumstances the dowel action mechanism can provide an important contribution to the shear transfer in cracked reinforced concrete. In most cases, however, the direction of the principal stress after cracking deviates only slightly from its direction during cracking. Then, the dowel action mechanism is of minor importance due to the relatively high axial steel stress.

7 Notation

a, b	numerical constants
a_x	projected contact area in x-direction [mm^2]
a_y	projected contact area in y-direction [mm^2]
e	eccentricity [mm]
f_{ccyl}	cylindrical concrete crushing strength [MPa]
f_{ccm}	cube concrete crushing strength [MPa]
f_{sy}	steel yield strength [MPa]
h	element size [mm]
m	numerical constant
n	number of cycles
n_f	number of cycles till failure
p_k	volume of the particles/total volume
r	radius [mm]
x	length [mm]
x	direction in the two-dimensional space
y	direction in the two-dimensional space
z	distance to neutral axis [mm]
A	cross-sectional area [mm^2]
A_x	total projected contact area in x-direction [mm^2]
A_y	total projected contact area in y-direction [mm^2]
C	numerical constant
D_{max}	maximum particle diameter [mm]
D_0	specific particle diameter [mm]
E_c	modulus of elasticity of concrete [MPa]
E_s	modulus of elasticity of steel [MPa]
F_d	dowel force [kN]
F_{du}	ultimate dowel force [kN]
G	shear modulus [MPa]
I	moment of inertia [mm^4]
K	numerical constant
$K_{1,\ldots,4}$	dowel stiffness [N/mm]
K_f	foundation modulus of concrete [MPa/mm]
L	length [mm]
M_u	ultimate bending moment [Nm]
P	numerical constant
α	angle of inclination
γ_a	retention factor of the stresses due to aggregate interlock
γ_d	retention factor of the stresses due to dowel action
γ_k	retention factor of the dowel stiffness
δ_t	shear displacement [mm]
δ_0	residual shear displacement [mm]

δ_m maximum shear displacement [mm]
$\delta_{t,e}$ shear displacement due to elastic deformation [mm]
δ_n crack width [mm]
$\delta_{n,0}$ initial crack width [mm]
ε numerical constant
$\lambda_{x,\ldots,y}$ retention factors of the contact areas
μ coefficient of friction
ϱ reinforcement ratio
σ normal stress [MPa]
σ_a normal stress due to aggregate interlock [MPa]
σ_d normal stress due to dowel action [MPa]
σ_s steel stress [MPa]
σ_{pu} strength of material [MPa]
σ_n normal stress acting upon the crack plane [MPa]
τ_a shear stress due to aggregate interlock [MPa]
τ_b bond stress [MPa]
τ_d shear stress due to dowel action [MPa]
τ_0 minimum applied shear stress [MPa]
τ_m maximum applied shear stress [MPa]
τ_u shear strength [MPa]
θ angle of inclination
ϕ bar diameter [mm]
ψ angle of friction

8 Literature

1. Bennett, E. W. and S. Banerjee, Strength of beam-column connections with dowel reinforcement, The Structural Engineer, Vol. 51, No. 4, April 1976, pp. 133–139.
2. Birkeland, P. W. and H. W. Birkeland, Connections in precast concrete constructions, ACI-journal, Vol. 63, No. 3, March 1966, pp. 345–368.
3. Chung, H. W., Shear strength of concrete joints under dynamic loads, Concrete, Vol. 12, March 1978, pp. 27–29.
4. Colley, B. E. and H. A. Humprey, Aggregate interlock at joints in concrete pavements, Highway Research Record, No. 189, 1967, pp. 1–18.
5. Daschner, F. and H. Kupfer, Versuche zur Schubkraftübertragung in Rissen von Normal- und Leichtbeton, Bauingenieur 57, (1982), pp. 57–60.
6. Daschner, F. and I. Nissen, Schubkraftübertragung in Rissen von Normal- und Leichtbeton, Betonwerk und Fertigteiltechnik, Vol. 53, Heft 1, 1987, pp. 45–51.
7. Divakar, M. P., A. Fafitis and S. P. Shah, A constitutive model for shear transfer in cracked concrete, submitted for publication, ASCE, Structural division 1987.
8. Dulacska, H., Dowel action of reinforcement crossing cracks in concrete, ACI-Journal, Vol. 69, Dec. 1972, pp. 754–757.
9. Eleiott, A. F., An experimental investigation of shear transfer across cracks in reinforced concrete, M.S. Thesis, Cornell University, Ithaca, June 1974.
10. Fenwick, R. C. and T. Paulay, Mechanism of shear resistance of concrete beams, ASCE, Structural Division, Vol. 94, No. 10, Oct. 1968, pp. 2325–2350.

11. FRENAY, J. W., G. LIQUI LUNG and A. F. PRUIJSSERS, Shear transfer across a single crack in reinforced concrete, Additional detailed tests, Report 5-86-5, Stevin Laboratory, Delft University of Technology, 1986, pp. 106.
12. FRIBERG, B. F., Design of dowels in transverse joints of concrete pavements, Transactions, ASCE, Vol. 105, 1940, pp. 1078–1080.
13. GERWICK, B. C., High strength concrete, key to the Arctic and deep sea, Proceeding of the conference on high strength concrete, Stavanger 1987, pp. 393–404.
14. HOFBECK, J. A., I. O. IBRAHIM and A. H. MATTOCK, Shear transfer in reinforced concrete, ACI-Journal, Vol. 66, Febr. 1969, pp. 119–128.
15. HOUDE, J. and M. S. MIRZA, A finite element analysis of shear strength of reinforced concrete beams, ACI-Special Publication 42, "Shear in reinforced concrete", pp. 103–128.
16. JIMENEZ, R., P. GERGELY and R. N. WHITE, Shear transfer across cracks in reinforced concrete, Report No. 78-4, Dept. of Structural Eng., Cornell University, Ithaca, Aug. 1978, pp. 357.
17. JIMENEZ, R., P. PERDIKARIS and P. GERGELY, Interface shear transfer and dowel action in cracked reinforced concrete subject to cyclic shear, Proceeding of the ASCE conference, Madison, Aug. 1976, pp. 457–475.
18. KLEIN, D., R. KRISTJANSSON, J. LINK, G. MEHLHORN and H. SCHAEFFER, Zur Berechnung von dünnen Stahlbetonplatten bei Berucksichtigung eines wirklichkeitsnahen Werkstoffverhaltens, Forschungsbericht No. 25, Inst. für Massivbau, Technische Hochschule Darmstadt, 1975, pp. 1–28.
19. LAIBLE, J. P., An experimental investigation of interface shear transfer and applications in the dynamic analysis of nuclear containment vessels, Dissertation, Cornell University, Ithaca, 1973, pp. 343.
20. LAIBLE, J. P., R. N. WHITE and P. GERGELY, Experimental investigation of seismic shear transfer across cracks in concrete nuclear containment vessels, ACI-Special Publication 53, Reinforced concrete structures in seismic zones, 1977, pp. 203–226.
21. MAST, R. F., Auxiliary reinforcement in concrete connections, ASCE, Journal of Structural Division, Vol. 94, No. 6, June 1968, pp. 1485–1499.
22. MATTOCK, A. H., Shear transfer in concrete having reinforcement at an angle to the shear plane, ACI-Special Publication 42, Shear in reinforced concrete, Vol. 1, 1974, pp. 17–42.
23. MATTOCK, A. H., Effect of aggregate type on single direction shear transfer strength in monolithic concrete, Report SM 74-2, Dept. of Civil Eng., University of Washington, Seattle, Washington, Aug. 1974.
24. MATTOCK, A. H., Cyclic shear transfer and type of interface, ASCE, Journal of Structural Division, Vol. 107, No. 10, Oct. 1981, pp. 1945–1964.
25. VAN MIER, J. G. M., Strain-softening of concrete under multiaxial loading conditions, Dissertation, University of Technology, Eindhoven, 1984, pp. 349.
26. MILLARD, S. G. and R. P. JOHNSON, Shear transfer across cracks in reinforced concrete due to aggregate interlock and dowel action, Mag. of Concrete Research, Vol. 36, No. 126, March 1984, pp. 9–21.
27. MILLARD, S. G. and R. P. JOHNSON, Shear transfer in cracked reinforced concrete, Mag. of Concrete Research, Vol. 37, No. 130, March 1985, pp. 3–15.
28. MILLS, G. M., A partial kinking yield criterion for reinforced concrete slabs, Mag. of Concrete Research, Vol. 27, No. 90, March 1975, pp. 13–22.
29. MOE, J., Discussion of "Shear and diagonal tension", by ACI-ASCE committee 326, Proceedings ACI, Vol. 59, No. 9, Sept. 1962, pp. 1334–1339.
30. NISSEN, I., Rissverzahnung des Betons, gegenseitige Rissuferverschiebungen und übertragene Kräfte, Dissertation, Technische Universität München, 1987, 214 pp.
31. PAULAY, T. and P. J. LOEBER, Shear transfer by aggregate interlock, ACI-Special Publication 42, "Shear in reinforced concrete", pp. 1–15.
32. PAULAY, T., R. PARK and M. H. PHILIPS, Horizontal construction joints in cast in place reinforced concrete, ACI-Special Publication SP-42, Shear in reinforced concrete, Vol. II, 1974, pp. 599–616.

33. PRUIJSSERS, A. F. and G. Liqui Lung, Shear transfer across a crack in concrete subjected to repeated loading, Experimental results, Part I, Report 5-85-12, Stevin Laboratory, Delft University of Technology, 1985, pp. 178.
34. PRUIJSSERS, A. F., Aggregate interlock and dowel action under monotonic and cyclic loading, Dissertation, Delft University of Technology, 1988, pp. 192.
35. RASMUSSEN, B. H., Strength of transversely loaded bolts and dowels cast into concrete, Laboratoriet for Bugningastatik, Denmark Technical University, Meddelelse, Vol. 34, No. 2, 1962, (in Danish).
36. STANTON, J. F., An investigation of dowel action of the reinforcement of nuclear containment vessels and their non-linear dynamic response to earthquake loads, M.S. Thesis, Cornell University, Jan. 1977.
37. The structural design of concrete pavements, Pt. 4, Public Roads, Sept. 1936.
38. TAYLOR, H. P. J., Fundamental behaviour in bending and shear of reinforced concrete, Thesis, London, 1971.
39. TAYLOR, R., A note on the mechanism of diagonal cracking in reinforced concrete beams without web reinforcement, Mag. of Concrete Research, Vol. 111, No. 31, March 1959, pp. 151–158.
40. TELLER, L. W. and E. J. SUTHERLAND, A study of structural action of several types of transverse and longitudinal joint design, Public Roads, Vol. 17, No. 7, Sept. 1936.
41. TERMONIA, Y. and P. MEAKIN, Formation of fractal cracks in a kinetic fracture model, Nature, Vol. 20, April 1986, pp. 429–431.
42. TIMOSHENKO, S. and J. M. LESSELS, Applied elasticity, Westinghouse Technical Night School Press, East Pittsburg, 1925.
43. TML technical bulletin No. 1007, Tokyo Sokki Instruments, The Hague, 1985.
44. UNTRAUER, R. E. and R. L. HENRY, Influence of normal pressure on bond strength, ACI-Journal, Vol. 62, No. 5, May 1965, pp. 557–586.
45. UTESCHER, G. and M. HERRMANN, Versuche zur Ermittlung der Tragfähigkeit in Beton eingespannter Rundstahldollen aus nichtrostendem austenitischem Stahl, Deutscher Ausschuss für Stahlbeton, Heft 346, Berlin, 1983, pp. 49–104.
46. VINTZELEOU, E N., Mechanisms of load transfer along reinforced concrete interfaces under monotonic and cyclic actions, Ph.D. Thesis (in Greek), Department of Civil Eng., National Technical University of Athens, December 1984, pp. 549.
47. VINTZELEOU, E. and T. P. TASSIOS, Mechanisms of load transfer along interfaces in reinforced concrete, prediction of shear force versus shear displacement curves, Studi e ricerche, Vol. 7, 1985, pp. 121–159.
48. VINTZELEOU, E. and T. P. TASSIOS, Mathematical models for dowel action under monotonic and cyclic conditions, Mag. of Concrete Research, Vol. 38, No. 134, March 1986, pp. 13–22.
49. VINTZELEOU, E. and T. P. TASSIOS, Behaviour of dowels under cyclic deformations, ACI, Structural journal, Vol. 84, Jan.-Febr. 1987, pp. 18–30.
50. WALRAVEN, J. C., Aggregate interlock, a theoretical and experimental analysis, Dissertation, Delft University of Technology, Oct. 1980, pp. 197.
51. WALRAVEN, J. C., The behaviour of cracks in plain and reinforced concrete subjected to shear, Final report of the IABSE colloquium Delft, 1981, pp. 227–245.
52. WALRAVEN, J. C., Kornverzahnung bei zyklischer Belastung, Mitteilungen aus dem Inst. für Massivbau der Techn. Hochschule Darmstadt, Heft 36, 1986, pp. 45–58.
53. WALRAVEN, J. C., J. FRENAY and A. F. PRUIJSSERS, Influence of concrete strength and load history on the shear friction capacity of concrete members, PCI-Journal, Vol. 32, No. 1, Jan./Febr. 1987, pp. 66–85.
54. WALRAVEN, J. C., E. Vos and H. W. REINHARDT, Experiments on shear transfer in cracks in concrete. Part I, Description of results, Report No. 5-79-3, Jan. 1979, Stevin Laboratory, Delft University of Technology.
55. WHITE, R. N. and M. J. HOLLEY, Experimental study of membrane shear transfer, ASCE, Structural Division, Vol. 98, No. 8, Aug. 1972, pp. 1835–1853.

APPENDIX I

Mix proportions

Mix code B1632550 strength $f'_{cc} = 51$ N/mm^2 (mix A)

components	[kg/m^3]	sieve analysis of aggregate: sieve opening [mm]	[kg]
sand	877.2	8 -16	623.7
gravel	1065.0	4 - 8	441.3
cement-B	325.0	2 - 4	312.1
		1 - 2	220.9
water	162.5	0.5 - 1	156.2
		0.25- 0.5	110.3
	2429.7	0.10- 0.25	77.7
			1942.2

Mix code B1642037.5 strength $f'_{cc} = 70$ N/mm^2 (mix B)

components	[kg/m^3]	sieve analysis of aggregate: sieve opening [mm]	[kg]
sand	857.3	8 -16	596.5
gravel	1018.5	4 - 8	421.9
cement-B	420.0	2 - 4	298.3
water	147.0	1 - 2	212.0
superpl. 2½%	10.5	0.5 - 1.0	148.6
		0.25- 0.50	105.0
	2453.3	0.10- 0.25	93.5
			1875.8

Sieve analysis of aggregate [cum.%]

mix A	mix B	Fuller	sieve opening [mm]
100.0	100.0	100.0	8 -16
67.9	68.2	70.7	4 - 8
45.2	45.7	50.0	2 - 4
29.1	29.8	35.4	1 - 2
17.7	18.5	25.0	0.5 - 1
9.7	10.6	17.7	0.25- 0.5
4.0	5.0	12.5	0.1 - 0.25

APPENDIX II

Experimental results

Table 3.1. Test results of mix A

code	f_{ccm} [N/mm^2]	τ_u [N/mm^2]	τ_m [N/mm^2]	τ_m/τ_u	No. of cycles	failure during cycling
A/4L/.61/6.1/.03	54.47	10.00	6.1	.610	455000	no
A/4L/.63/6.0/.06	50.20	9.47	6.0	.634	263337	no
A/4H/.64/7.0/.06	54.30	10.97	7.0	.638	368000	no
A/4L/.65/6.0/.01	46.83	9.29	6.0	.646	34000	no
A/4H/.66/6.9/.02	50.99	10.50	6.9	.657	550000	no
A/4L/.70/7.0/.01	54.49	10.00	7.0	.700	2410	no
A/4L/.73/7.2/.05	53.70	9.90	7.2	.727	14000	yes
A/4L/.74/7.0/.01	49.85	9.42	7.0	.743	435	no
A/4L/.76/7.0/.02	48.20	9.20	7.0	.761	5925	yes
A/4H/.76/7.7/.03	48.50	10.15	7.7	.759	4762	yes
A/4L/.77/7.2/.04	49.48	9.38	7.2	.768	1785	yes
A/4H/.78/8.0/.04	49.30	10.26	8.0	.780	5198	yes
A/4L/.79/8.6/.02	53.47	10.86	8.6	.792	895	yes
A/4L/.80/7.3/.03	47.20	9.09	7.3	.803	1192	yes
A/4L/.80/7.5/.05	49.60	9.39	7.5	.799	299450	yes
A/4L/.82/7.4/.05	46.43	8.99	7.4	.823	996	yes
A/4L/.90/9.0/.05	54.50	10.00	9.0	.900	118	yes
A/6L/.51/6.0/.04	51.37	11.89	6.0	.505	508000	no
A/6L/.56/6.7/.05	51.41	11.90	6.7	.563	386000	yes
A/6L/.58/6.8/.01	50.40	11.73	6.8	.578	194000	no
A/6L/.61/7.2/.04	51.30	11.88	7.2	.606	160300	no
A/6L/.62/8.0/.04	57.30	12.89	8.0	.621	410781	no
A/6H/.66/7.9/.03	45.10	11.84	7.9	.663	1750	yes
A/6L/.66/8.6/.02	58.60	13.10	8.6	.656	40722	yes
A/6L/.67/8.2/.08	53.20	12.20	8.2	.672	21000	yes
A/6L/.68/8.0/.03	51.04	11.83	8.0	.676	1000	yes

Table 3.2. Test results of mix B

code	f_{ccm} [N/mm^2]	τ_u [N/mm^2]	τ_m [N/mm^2]	τ_m/τ_u	No. of cycles	failure during cycling
B/4L/.57/7.0/.03	73.54	12.27	7.0	.570	665000	no
B/4L/.59/7.0/.20	69.90	11.85	7.0	.591	1331	yes
B/4L/.60/7.0/.06	69.46	11.74	7.0	.596	512660	no
B/4L/.60/7.4/.08	73.54	12.27	7.4	.603	82500	yes
B/4L/.61/7.3/.04	70.80	11.95	7.3	.611	23500	yes
B/4H/.61/8.5/.04	75.34	13.89	8.5	.612	355716	no
B/4L/.63/7.3/.04	67.89	11.61	7.3	.629	931731	yes
B/4L/.65/8.0/.07	73.47	12.26	8.0	.653	62000	yes
B/4H/.66/9.0/.04	74.00	13.69	9.0	.657	2224	yes
B/4L/.75/8.4/.05	65.10	11.28	8.4	.745	219029	yes
B/4L/.79/8.8/.08	63.88	11.11	8.8	.792	1150	yes
B/4L/.81/9.1/.04	64.70	11.23	9.1	.810	1441	yes
B/6L/.46/6.9/.04	70.70	15.11	6.9	.457	550000	no
B/6L/.52/7.9/.02	71.70	15.26	7.9	.518	290000	no
B/6L/.53/8.0/.06	71.40	15.21	8.0	.526	250000	no
B/6L/.56/8.9/.02	75.10	15.81	8.9	.563	325900	no

Table 3.3. Comparison of the theoretical and the experimental static shear strength

code	τ_u [N/mm^2]	$\tau_{u,th}$ [N/mm^2]	$\tau_u/\tau_{u,th}$
A/4L/.61/6.1/.03	10.00	10.17	0.98
A/4L/.63/6.0/.06	9.47	10.10	0.94
A/4H/.64/7.0/.06	10.97	11.77	0.93
A/4H/.66/6.9/.02	10.50	12.44	0.84
A/6L/.51/6.0/.04	11.89	12.10	0.98
A/6L/.58/6.8/.01	11.73	11.21	1.05
A/6L/.61/7.2/.04	11.88	12.30	0.97
A/6L/.62/8.0/.04	12.89	12.48	1.03
B/4L/.60/7.0/.06	11.74	10.60	1.11
B/4H/.61/8.5/.04	13.89	12.66	1.10
B/6L/.46/6.9/.04	15.11	13.50	1.12
B/6L/.52/7.9/.02	15.26	14.27	1.07
B/6L/.56/8.9/.02	15.81	15.99	0.99
average ratio = 1.01, $s = 0.08$			

Table 3.4. Experimental results of plain concrete specimens

code	f_{ccm} [N/mm^2]	σ_0 [N/mm^2]	τ_m [N/mm^2]	No. of cycles	failure during cycling
A/1.3/4.0/.12	51.53	1.30	4.0	30800	yes
A/1.2/5.0/.01	52.06	1.22	5.0	20326	no
A/1.3/5.0/.01	54.60	1.27	5.0	3080	yes
A/1.9/5.0/.19	48.40	1.90	5.0	9756	yes
A/0.8/5.5/.01	49.56	0.80	5.5	1520	yes
A/2.1/6.1/.01	54.53	2.14	6.1	8640	yes
A/1.3/6.2/.01	48.09	1.34	6.2	283549	yes
A/1.3/6.2/.02	52.57	1.26	6.2	3120	yes
B/1.1/5.0/.04	71.64	1.07	5.0	254369	no
B/1.2/5.6/.01	68.36	1.15	5.6	89500	no
B/1.0/6.2/.04	72.25	0.99	6.0	2736	yes
B/2.0/6.5/.01	69.14	2.02	6.5	343	yes
B/3.6/6.9/.19	70.20	3.58	6.9	82378	no
B/1.5/7.7/.01	67.54	1.99	7.7	3970	yes